AIAA JOURNAL
Vol. 55, No. 6, June 2017

Computational Dynamics of Flapping Wings in Hover Flight: A Co-Simulation Strategy

Bruno A. Roccia* and Sergio Preidikman†
National University of Córdoba, 5000 Córdoba, Argentina
and
Balakumar Balachandran‡
University of Maryland, College Park, Maryland 20742

DOI: 10.2514/1.J055137

A co-simulation strategy for modeling the unsteady dynamics of flying insects and small birds as well as biologically inspired flapping-wing micro-air-vehicles is developed in this work. In particular, the dynamic system under study is partitioned in two subsystems (the structural model and the aerodynamic model) that exchange information in a strong way. The vehicle or insect system is modeled as a collection of rigid bodies and lifting surfaces that can undergo deformations such as spanwise twisting, in-plane bending, out-of-plane bending, and an arbitrary combination of these deformation mechanisms. To account for the loads associated with the airflow, an aerodynamic model based on an extended version of the unsteady vortex-lattice method is used. The motion equations are integrated by using a fourth-order predictor-corrector method along with a procedure to stabilize the solution of the resulting differential-algebraic equations. The numerical results obtained for the unsteady lift and dynamics of a fruit fly in free hover flight are found to be in close agreement with prior experimental results reported in the literature. Furthermore, the inclusion of an adequate wing deformation pattern results in an increase of the lift force compared with that of a rigid wing surface, pointing to the importance of wing flexibility on aerodynamic performance. From the findings reported in this paper, it is believed that the numerical simulation framework presented here could serve as a computational tool for further studies of flying insects and micro-air-vehicles.

Downloaded by UNIVERSITY OF MARYLAND on June 12, 2017 | http://arc.aiaa.org | DOI: 10.2514/1.J055137

Nomenclature

A_i^k	=	area of ith aerodynamic panel belonging to kth body
$\boldsymbol{B}_{q_k}$	=	Jacobian tensor of constraints associated with set of coordinates $\mathbf{q}_k$
$\{{}^k\hat{\boldsymbol{b}}_1, {}^k\hat{\boldsymbol{b}}_2, {}^k\hat{\boldsymbol{b}}_3\}$	=	right-handed orthonormal kth body-fixed frame
c	=	wing chord length
$\hat{\boldsymbol{e}}_i^k$	=	unit vector at control point of, and normal to, ith aerodynamic panel belonging to kth body
$\mathbf{G}_k$	=	rotation parameterization matrix for kth body
$H_k^j(\eta)$	=	eigenfunction
$\boldsymbol{h}(\tilde{\boldsymbol{z}}_{n+1}; t_{n+1})$	=	invariant set for index 1 DAE system
$\mathbf{I}_3$	=	3×3 identity matrix
$\mathbf{L}$	=	stabilization matrix
$\mathbf{M}_k$	=	primary motion mass matrix for kth body
$\mathbf{N}_k$	=	shape function matrix for kth body
n_c	=	number of constraint equations
n_{coord}	=	number of nonindependent absolute coordinates
n_{DOF}	=	number of degrees of freedom
n_p	=	number of panels of aerodynamic grid
n_f, T_f	=	flapping frequency and flapping period
$\{\hat{\boldsymbol{n}}_1, \hat{\boldsymbol{n}}_2, \hat{\boldsymbol{n}}_3\}$	=	right-handed orthonormal inertial/Newtonian frame
$p(x;t), p_\infty$	=	unknown pressure and pressure far away from body
$\mathbf{p}_k$	=	array containing elastic generalized coordinates
$p_k^j(t)$	=	elastic generalized coordinate
$\boldsymbol{Q}_{\text{NB}^k}$	=	rotation tensor from kth body-fixed frame to inertial frame
$\boldsymbol{Q}_k$	=	generalized load vector comprising conservative and nonconservative loads
$\mathbf{Q}_k^{\text{aero}}$	=	aerodynamic generalized loads for kth body
$\mathbf{Q}_k^{\text{grav}}$	=	generalized loads due to gravitational field for kth body
$\mathbf{q}_k, \dot{\mathbf{q}}_k$	=	set of absolute coordinates for kth body and its time derivative
$\dot{\boldsymbol{R}}_k$	=	velocity associated with origin of kth body-fixed frame
$\dot{\boldsymbol{R}}_k^P$	=	absolute velocity vector for arbitrary point belonging to kth body
$\boldsymbol{r}_k$	=	position vector of arbitrary point P on kth body in undeformed configuration
$\bar{\boldsymbol{r}}_k, \bar{\boldsymbol{u}}_k$	=	skew-symmetric tensors associated with $\boldsymbol{r}_k$ and $\boldsymbol{u}_k$
$\boldsymbol{s}_k^{P'P}$	=	position vector of point P relative to point P'
T_k	=	kinetic energy of kth body
t	=	dimensional time
$\mathbf{u}_k$	=	elastic displacement vector of point P
$\mathbf{u}_k^{P'}$	=	elastic displacement vector associated with point P' resolved in given reference basis
$\boldsymbol{V}_\infty$	=	free-stream velocity
$\boldsymbol{V}(\mathbf{x};t)$	=	velocity field

Received 22 February 2016; revision received 31 October 2016; accepted for publication 1 February 2017; published online 27 April 2017. Copyright © 2017 by the American Institute of Aeronautics and Astronautics, Inc. All rights reserved. All requests for copying and permission to reprint should be submitted to CCC at www.copyright.com; employ the ISSN 0001-1452 (print) or 1533-385X (online) to initiate your request. See also AIAA Rights and Permissions www.aiaa.org/randp.

*Associate Professor, Structures Department, School of Exact, Physical, and Natural Sciences; also Group of Applied Mathematics, National University of Rio Cuarto, Cordoba, Argentina 5800; Institute for Advanced Studies in Engineering and Technology, National Scientific and Technical Research Council IDIT-CONICET, Córdoba, Argentina 5000; bruno.roccia@gmail.com. Member AIAA.

†Professor, Structures Department, School of Exact, Physical, and Natural Sciences; also Group of Applied Mathematics, National University of Rio Cuarto, Cordoba, Argentina 5800; Institute for Advanced Studies in Engineering and Technology, National Scientific and Technical Research Council IDIT-CONICET, Córdoba, Argentina 5000. Member AIAA.

‡Minta Martin Professor, Department of Mechanical Engineering. Fellow AIAA.

$W(t)$ = total energy per unit mass
x = position vector of a fluid particle at instant t
x_{node}, v_{node} = position and velocity of aerodynamic panel corner
$\varphi(\mathbf{x}, t)$ = potential velocity
$\Gamma(t)$ = circulation associated with finite segment of vortex line
ρ, ρ_{oil} = constant density and density of oil used in robofly experiment
$\tilde{z}_{n+1}$ = solution computed by Hamming's method
$\mathfrak{B}_k$ = secondary motion mass matrix for kth body
$\mathfrak{M}_k$ = mass matrix that couples primary and secondary motions
Δp_i^k = pressure jump for ith aerodynamic panel belonging to kth body
$\boldsymbol{\lambda}_k$ = vector of Lagrange's multipliers for kth body
$\boldsymbol{\omega}_k$ = angular velocity vector of kth body-fixed frame relative to inertial frame
ρ_k = mass density per unit of volume
$\dot{\boldsymbol{\theta}}_k$ = array of time derivative of rotation parameters for kth body
$\boldsymbol{\varphi}_k = (\varphi_k^1, \varphi_k^2, \varphi_k^3)^T$ = small rotations due to deformations on elastic axis
$\boldsymbol{\Phi}_k$ = set of algebraic constraint equations

I. Introduction

IN RECENT years, drawing inspiration from flapping wings in nature, many studies have focused on studies and design of micro-air-vehicles (MAVs). Such flying systems, wherein flow separations take place on highly flexible structural members undergoing complex motions, are difficult to analytically study. The governing equations of motion form a nonlinear system, which is characterized by a fully unsteady three-dimensional (3D) flow strongly coupled with the MAV structure. A complete numerical model intended for flapping wings would need the following: 1) precise information on wing kinematics, 2) an aerodynamic model able to accurately predict the loads acting on the lifting surfaces, 3) a nonlinear hybrid dynamic model for the rigid–flexible MAV's structure able to predict its structural response under excitation of aerodynamic loads; 4) a control system able to suppress undesirable motions and optimize its performance under different flow conditions; 5) a technique for transferring information between the aerodynamic and structural models; and 6) an integration scheme to solve all the governing equations, which in the most general case are differential algebraic in nature.

Early attempts to understand the aerodynamics of flapping wings relied on experimental investigations, which were used for measuring the time histories of aerodynamic forces in tethered insects [1–4]. Recently, the development and availability of significant computing capabilities supress has enabled investigations based on viscous flow solvers, such as 3D Navier–Stokes models [5]; Reynolds-averaged Navier–Stokes (RANS) codes [6,7]; arbitrary Lagrangian Eulerian (ALE) formulations [8]; and direct numerical simulations (DNS) solvers [9], among others. However, significant computational difficulties and cost associated with the use of models based on computational fluid dynamics (CFD) techniques have led to alternative approaches; some of them have been extensively used in aircraft studies, for example, the unsteady vortex-lattice method (UVLM) [10]. Lately, UVLM has been gaining ground in the study of nonstationary problems, where free-wake methods become necessary in problems involving highly flexible complex geometries undergoing arbitrary motions such as flying vehicles inspired by biology [10–16].

With respect to dynamics of flapping wings, different studies have been performed through the years; at the beginning, most of them were based on the standard aircraft six-degree-of-freedom equations [17,18]. Considerable research has been conducted in this field on several insect species and diverse MAV prototypes by using the same technique. However, in all of them, mass of the wings and the associated inertial effects are neglected [19–25]. Many improved dynamic models have been developed in order to carry out numerical studies on the dynamic behavior of flying insects and MAVs like flapping wings, such as follows: two-dimensional (2D) approaches based on articulated rigid mechanisms coupled with Navier–Stokes solvers [26] and UVLM versions [27]; the work of Khan and Agrawal [28] in which three-degree-of-freedom wings are considered; studies based on the Newton–Euler equations [29,30]; dynamics based on the Gibbs–Appel equations considering the inertial/mass effects of the wings on the MAV's fuselage [31,32]; and models found in multibody approaches based on Boltzman–Hamel equations [33] and Kane's equations [34], among others. More recently, Orlowski and Girard [35] presented an extensive literature review for dynamic models of flapping wings. In addition, these authors carried out numerical simulations by using a six-degree-of-freedom model that allowed them to conclude the importance of considering the inertial coupling between the vehicle system's fuselage and wings.

However, in most of the previously mentioned efforts, the focus has been on dynamics, control, and stability, with the lift and drag forces being computed by steady or quasi-steady aerodynamic models. From this literature review, it is clear that there is a need for an integral study involving nonlinear dynamics and unsteady aerodynamics of flying insects and/or MAVs. To address this gap, a numerical framework well suited for studying the dynamics of both flying insects as well as flapping-wing MAVs is presented in this paper. The entire system under study is partitioned in two subsystems (the MAV/insect structure model and the aerodynamic model) that can exchange information in a strong way. From this point of view, the computational environment built can be seen as a sort of *strong co-simulation framework* [36]. The aforementioned subsystems consist of a dynamically nonlinear model based on an extended version of [37], which allows us to impose different deformation patterns on the insect's wings (i.e., all deformations are prescribed by means of known functions of time), such as spanwise twisting, out-of-plane bending, in-plane bending, and an arbitrary combination of these deformation fields. To take aerodynamic loads into account, this hybrid dynamic model and an aerodynamic model based on a modified version of the nonlinear UVLM [16] are coupled by the authors. Such a model takes all possible aerodynamic interferences into account and allows for obtaining the following information: 1) flow field around the structure, 2) spatial-temporal vorticity distribution attached to the structure, 3) vorticity distribution in the wakes emanating from the sharp edges of lifting surfaces, 4) positions and shapes of wakes, and 5) unsteady aerodynamic loads acting on the wings.

In addition, the authors also describe a numerical procedure to solve all the governing equations, which originally form a differential algebraic system of index 3. This set of equations is rewritten as a system of index 1 through an index reduction technique and integrated simultaneously in the time domain. Such an integration is achieved by means of a fourth-order scheme based on the modified method of Hamming [38,39] combined with a procedure to control/eliminate the numerical drift that results as consequence of the index reduction. *To the best of the authors' knowledge, a study of nonlinear dynamics and unsteady aerodynamics of flying insects and MAVs, based on a multibody system approach in combination with the UVLM involving free-deforming wakes, time-dependent geometries, and largely attached flows is unavailable in the current literature; this computational dynamics is the primary focus of the present work.*

The rest of this paper is organized as follows: In Sec. II, a brief revision of the UVLM is presented. In Sec. III, a detailed formulation of the nonlinear dynamic model of the MAV is presented. This is followed by a description of the co-simulation strategy, the numerical integration scheme, and the poststabilization technique adopted to suppress the numerical drift. In Sec. V, the nonlinear dynamic-unsteady aerodynamic models are validated by comparing numerical results with available analytical and experimental data. As an

Downloaded by UNIVERSITY OF MARYLAND on June 12, 2017 | http://arc.aiaa.org | DOI: 10.2514/1.J055137

illustration of the co-simulation capabilities presented here, a study on a free-flying insect (fruit fly) in hovering flight is conducted. The limitations of the current framework are also discussed. Finally, to close the paper, concluding remarks and thoughts of future works are collected together in Sec. VI.

II. Model for Aerodynamics

An extended and modified version of the general method known as UVLM is used in this work. This method can be applied to 3D lifting and nonlifting surfaces. The surface of the body may undergo arbitrary time-dependent deformations and can execute any type of maneuver in space. The flow around the body, that is, the fuselage and wings of the MAV, is assumed to be irrotational and incompressible over the entire flow field, except adjacent to the solid boundaries of the body and wakes. This approach allows one to consider nonlinear and unsteady aerodynamic effects associated with large angles of attack and static deformations. The UVLM scheme also allows one to take all possible aerodynamic interferences into account as well as estimate the spatial-temporal vorticity distribution attached to the body's surface, the vorticity distribution in the wakes shed from the sharp edges of the wings, as well as their locations and shapes.

In the proposed model, the authors consider a flow of an incompressible fluid characterized by a very high Reynolds number. Given that the Reynolds number characterizing insect flights is relatively low, a question naturally arises. Can one use UVLM reliably for predicting the aerodynamic loads on flapping wings? Dickinson et al. [40] and Dickinson and Götz [41] showed by means of experimental studies that viscous effects can be neglected in the range of Reynolds numbers 75–4000 for hovering MAVs/insects. Ramamurti and Sandberg [8] obtained similar conclusions by analyzing the effect of viscosity on the unsteady flow surrounding a 3D *Drosophila*'s wing undergoing flapping motion. Based on these observations, recently, Roccia et al. [16] have conducted a series of numerical studies on the aerodynamics of flapping wings by using a modified version of the UVLM. Their results show exceptionally good agreement in terms of trends and magnitude with the experimental data reported by Dickinson et al. [40]. These findings render the UVLM as an accurate and efficient numerical model for studies of aerodynamics of flying insects and MAVs.

A. Discretization of the Vortex Sheets

In the UVLM, the bound-vortex sheets are replaced by a lattice of short, straight vortex segments with circulation $\Gamma(t)$. These segments are used to divide the wing surface into a number of elements of area (the so-called *panels*). The model is completed by joining free vortex lines, representing free-vortex sheets, to the bound-vortex lattice along the separation edges, such as the trailing edges and leading edges of the lifting surfaces. The locations at which separation occurs are considered as input data, and they are not determined as part of the solution. However, the vortex lattices representing wakes (the positions of the vortex segments and the circulations around them) are determined as part of the solution.

B. Boundary Conditions

The governing equation of the problem is complemented with the following boundary conditions:

1) *Regularity at infinity:* This condition requires that all disturbances that characterize a moving body in a fluid, initially at rest, decay away from the body and its wakes.

2) *No-penetration condition:* It is applied over the entire boundary of the solid immersed in the fluid. This condition, which is also known as *impermeability*, requires that the normal component of the velocity of all fluid particles relative to the body surface must be zero on the body surface. This condition is imposed on the control points (CPs) located in the geometric center of each panel.

C. Aerodynamic Loads

The aerodynamics loads acting on the lifting surfaces are computed as follows: 1) for each element, the pressure jump at the control point is computed by integrating the unsteady Bernoulli Eq. (1); 2) the force on each element is calculated as the product of the pressure jump, the element area, and the unit vector normal to each aerodynamic panel; 3) the resultant forces and moments are computed as the (vector) summation of the forces and moments produced by each element.

Next, consider

$$\partial_t \varphi(\boldsymbol{x};t) + \frac{1}{2}\boldsymbol{V}(\boldsymbol{x};t)\cdot\boldsymbol{V}(\boldsymbol{x};t) + \frac{p(\boldsymbol{x};t)}{\rho} = W(t) \tag{1}$$

where ∂_t denotes the partial time derivative at a fixed space location in an inertial reference frame; $\boldsymbol{V}(\boldsymbol{x};t)$ is the spatial gradient of the velocity potential $\varphi(\boldsymbol{x};t)$; $p(\boldsymbol{x};t)$ is the unknown pressure; ρ is the constant density of the fluid; $W(t)$ is the total energy per unit mass, which depends only on time and has a unique value at every point of the whole fluid domain; and $\boldsymbol{x}$ is the position vector of a fluid particle at the instant t. In its present form, the evaluation of $\partial_t\varphi$ is troublesome, but this term can be stated so as to make its evaluation relatively easy. Detailed explanations of the treatment of each term in Eq. (1), as well as a full formulation of the UVLM, can be founded in the work of Konstandinopoulos et al. [42], Preidikman [39], Preidikman and Mook [38], and Roccia et al. [16]. The last mentioned reference contains all the extensions needed to attack the problem of flapping wings.

Once loads have been computed, each segment of the wakes is "convected" by means of convection of its end nodes to their new positions; this can be approximated as

$$\boldsymbol{x}_{\text{node}}(t+\Delta t) \approx \boldsymbol{x}_{\text{node}}(t) + \boldsymbol{v}_{\text{node}}(t)\Delta t \tag{2}$$

where $\boldsymbol{x}_{\text{node}}$ and $\boldsymbol{v}_{\text{node}}$ are the position and velocity of an aerodynamic panel corner, and Δt is the time step.

III. Model for Vehicle Dynamics

The computational model of the MAV adopted in this paper to study the dynamics as well as aerodynamics of flapping wings is based on the morphology of a fruit fly [43]. For simplicity, each part of the central body (head, thorax, and abdomen) is modeled as a surface of revolution [37]. The revolution surfaces that define the body as well as the wing surfaces are discretized by using simple quadrilateral elements with four nodes.

In this section, the governing equations for the vehicle system are developed considering large rotations and displacements in space, *primary motions*, and small/moderate rotations and displacements with respect to a reference frame, *secondary motions*. Basically, the primary motions are used to describe the position and orientation of each body as a whole in space, and the secondary motions are used to describe elastic movements if they exist.

The vehicle equations of motion are derived by means of Lagrange's equations for constrained systems. The MAV is modeled as a collection of three rigid and deformable bodies ($n_b = 3$). One of them, completely rigid (the central body), and the remaining two bodies, the wings, may undergo only prescribed deformation patterns. The location of each one of the three bodies in space is identified by using a set of six absolute Cartesian coordinates (three coordinates define the position of a fixed point on the body, and the others for the orientation of the body). This results in a total of 18 absolute nonindependent coordinates ($n_{\text{coord}} = 6n_b = 18$), which are linked through constraint equations. The wings undergo a prescribed motion (kinematically driven) with respect to the central body. This fact introduces 12 constraint equations ($n_c = 12$), 6 to specify the joint point between the central body and the wings and 6 to specify the orientation of the wings with respect to the central body. Thus, the number of degrees of freedom of the multibody system is six ($n_{\text{DOF}} = n_{\text{coord}} - n_c = 6$). In what follows, bold italic letters and

Downloaded by UNIVERSITY OF MARYLAND on June 12, 2017 | http://arc.aiaa.org | DOI: 10.2514/1.J055137

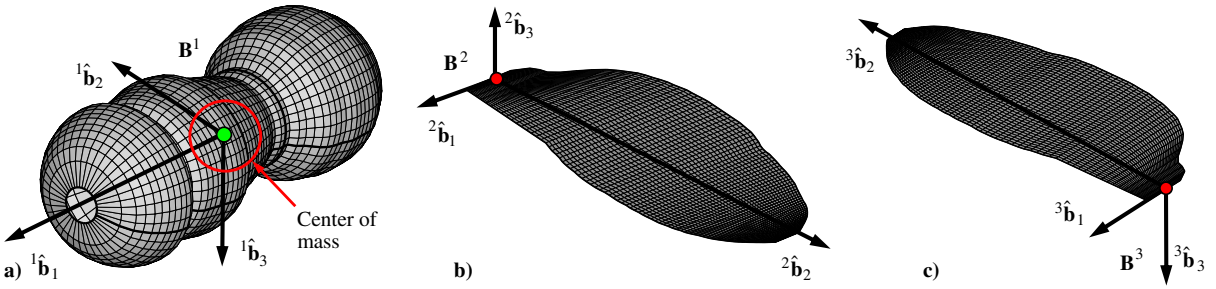

Fig. 1 Model representation and definition of reference frames: a) central body, b) left wing, and c) right wing.

bold letters are used for tensor notation and matrix notation, respectively.

A. Reference Frames and Absolute Coordinates

The authors use four reference systems (see Fig. 1): 1) a Newtonian or inertial system $\mathbf{N} = \{\hat{\boldsymbol{n}}_1, \hat{\boldsymbol{n}}_2, \hat{\boldsymbol{n}}_3\}$ and 2) a reference system fixed to each MAV's body denoted by $\mathbf{B}^k = \{{}^k\hat{\boldsymbol{b}}_1, {}^k\hat{\boldsymbol{b}}_2, {}^k\hat{\boldsymbol{b}}_3\}$. The reference frame $\mathbf{B}^1$ is a body-fixed frame attached at the center of mass of the central body, and the reference frames $\mathbf{B}^2$ and $\mathbf{B}^3$ are body-fixed frames attached to the left and right wings with origin at the wing joints.

The set of absolute coordinates for each body is given by

$$\mathbf{q}_k = (x_k, y_k, z_k, \phi_k, \theta_k, \psi_k)^T \quad \text{for } k = 1, 2, 3 \tag{3}$$

where x_k, y_k, and z_k are rectangular Cartesian coordinates associated to the unit vectors $\hat{\boldsymbol{n}}_1$, $\hat{\boldsymbol{n}}_2$, and $\hat{\boldsymbol{n}}_3$, respectively, and ϕ_k, θ_k, and ψ_k are angular coordinates that orientate the kth body relative to the inertial frame $\mathbf{N}$.

To orientate each body with respect to the inertial frame, the authors have used a rotation representation based on Euler angles [44]: a 2–3–1 rotation sequence for the central body and a 1–3–2 rotation sequence for each wing.

B. Velocity for an Arbitrary Point Belonging to a Body

Let us consider a flexible body that moves and deforms in space. The components of the absolute vector of translational velocity for an arbitrary point belonging to the body can be expressed in a segregated form. In this approach, the authors consider large rotations and displacements due to *primary motions*, and small rotations and displacements due to *secondary motions*. As the central body is entirely modeled as a rigid body, the expression for the absolute velocity vector for an arbitrary point is defined as ([44,45])

$$\dot{\boldsymbol{R}}_1^P = \dot{\boldsymbol{R}}_1 + \boldsymbol{Q}_{\mathrm{NB}^1}(\boldsymbol{\omega}_1 \times \boldsymbol{r}_1) \tag{4}$$

where $\dot{\boldsymbol{R}}_1$ is the velocity associated to the origin of the body-fixed frame $\mathbf{B}^1$, $\boldsymbol{r}_1$ is the position vector of an arbitrary point P on the central body, $\boldsymbol{\omega}_1$ is the angular velocity vector of $\mathbf{B}^1$ relative to the inertial frame $\mathbf{N}$, and $\boldsymbol{Q}_{\mathrm{NB}^1}:\mathbf{B}^1 \to \mathbf{N}$ represents a rotation tensor from the body-fixed frame $\mathbf{B}^1$ to the inertial frame $\mathbf{N}$.

Regarding the wings, they are allowed to deform according to pre-established deformation patterns; hence, the absolute velocity vector for an arbitrary point belonging to the left (right) wing is defined as

$$\dot{\boldsymbol{R}}_k^P = \dot{\boldsymbol{R}}_k + \boldsymbol{Q}_{\mathrm{NB}^k}[\dot{\boldsymbol{r}}_k + \dot{\boldsymbol{u}}_k + \boldsymbol{\omega}_k \times (\boldsymbol{r}_k + \boldsymbol{u}_k)], \quad \text{for } k = 2, 3 \tag{5}$$

Here, $\dot{\boldsymbol{R}}_k$ is the velocity associated with the origin of the body-fixed frame $\mathbf{B}^k$, $\boldsymbol{r}_k$ is the position vector of an arbitrary point P on the kth body at the undeformed configuration, $\dot{\boldsymbol{r}}_k$ is identically zero because the differentiation is performed with respect to the $\mathbf{B}^k$ frame, $\boldsymbol{u}_k$ is the elastic displacement vector of the point P and $\dot{\boldsymbol{u}}_k$ represents its first time derivative, ω_k is the angular velocity vector of the $\mathbf{B}^k$ relative to the inertial frame $\mathbf{N}$, and $\boldsymbol{Q}_{\mathrm{NB}^k}:\mathbf{B}^k \to \mathbf{N}$ represents a rotation tensor from the body-fixed frame $\mathbf{B}^k$ to the inertial frame $\mathbf{N}$. In Eq. (5), the values "2" and "3" for the subscripts "k" represent the left wing and right wing, respectively. After algebraic manipulations, Eqs. (4) and (5) can be written as

$$\dot{\boldsymbol{R}}_1^P = \dot{\boldsymbol{R}}_1 - \boldsymbol{Q}_{\mathrm{NB}^1}(\bar{\boldsymbol{r}}_1 \boldsymbol{\omega}_1) \tag{6}$$

$$\dot{\boldsymbol{R}}_k^P = \dot{\boldsymbol{R}}_k + \boldsymbol{Q}_{\mathrm{NB}^k}\dot{\boldsymbol{u}}_k - \boldsymbol{Q}_{\mathrm{NB}^k}[(\bar{\boldsymbol{r}}_k + \bar{\boldsymbol{u}}_k)\boldsymbol{\omega}_k], \quad \text{for } k = 2, 3 \tag{7}$$

where $\bar{\boldsymbol{r}}_1$, $\bar{\boldsymbol{r}}_k$, and $\bar{\boldsymbol{u}}_k$ are skew-symmetric tensors associated with $\boldsymbol{r}_1$, $\boldsymbol{r}_k$, and $\boldsymbol{u}_k$ respectively, in which their actions on vectors are equivalent to the action of cross products.

C. Wing Deformation Mechanism

As mentioned in Sec. I, all deformation patterns on the wings are prescribed as functions of time. This is achieved by means of a "virtual" beam element defined along the unit vector ${}^k\hat{\boldsymbol{b}}_2$; this provides the necessary means to bend and twist the wings in a desirable manner. The beam element adopted is an Euler–Bernoulli model, which is considered clamped at the wing root and free to move at the tip. Bending motion in two perpendicular planes (in plane and out of plane) is achieved by using expansions in terms of eigenfunctions, and the spanwise torsion is accounted by a linear interpolation function. The mechanism used to deform the wing consists of two steps: first, a deformation pattern is imposed on the virtual beam element (also called elastic axis), and, subsequently, the displacement field is transferred to the rest of the wing. In Figs. 2a and 2b, the authors show the location of the virtual beam element inside the wing and the position vector of an arbitrary point belonging to the wing at the undeformed configuration. Point P on the wing's surface and point P' on the elastic axis lie in the same plane, which is perpendicular to vector ${}^k\hat{\boldsymbol{b}}_2$ in the undeformed configuration (see Fig. 2a). The cross section of the wing that contains points P and P' is assumed to be rigid and the position vector of point P relative to point P' is denoted by $\boldsymbol{s}_k^{P'P}$ (see Fig. 2b).

After some algebraic manipulations and by expressing all of the results in the reference basis fixed to the kth body, the elastic displacement vector of an arbitrary point P on the wing can be written as

$$\mathbf{u}_k = \mathbf{u}_k^{P'} - \bar{\mathbf{s}}_k^{P'P}\boldsymbol{\varphi}_k, \quad \text{for } k = 2, 3 \tag{8}$$

where $\mathbf{u}_k^{P'}$ is the elastic displacement vector associated to point P' resolved in $\mathbf{B}^k$; $\boldsymbol{\varphi}_k = (\varphi_k^1, \varphi_k^2, \varphi_k^3)^T$ are small rotations due to deformations on the elastic axis; and $\bar{\mathbf{s}}_k^{P'P}$ is a skew-symmetric matrix associated with the column vector $\mathbf{s}_k^{P'P} = (s_k^1, s_k^2, s_k^3)^T$.

Each component of the elastic displacement vector $\mathbf{u}_k^{P'} = (u_k^1, u_k^2, u_k^3)^T$ is expressed as the product of an eigenfunction, $H_k^j(\eta)$, and a generalized temporal coordinate, $p_k^j(t)$, where η is the spatial coordinate along the elastic axis at the undeformed configuration. This can be written as

$$u_k^j(\eta; t) = H_k^j(\eta)\, p_k^j(t), \quad \text{for } j = 1, 2, 3 \tag{9}$$

The eigenfunctions $H_k^j(\eta)$ (for $j = 1, 2, 3$) are obtained by solving the differential equation that governs the free-vibration problem of an Euler–Bernoulli beam with clamped-free boundary conditions [46] (see Fig. 2c). The component $u_k^2(\eta; t)$, which accounts for axial

Downloaded by UNIVERSITY OF MARYLAND on June 12, 2017 | http://arc.aiaa.org | DOI: 10.2514/1.J055137

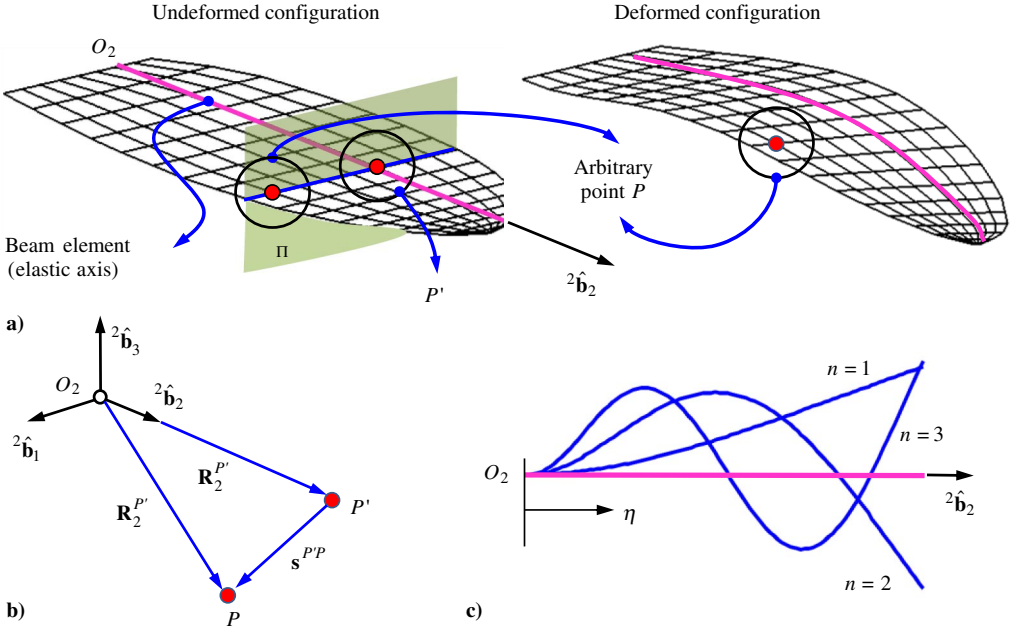

Fig. 2 a) Undeformed and deformed configurations of wing, b) definition of position vector of point P on wing in undeformed configuration, and c) eigenfunctions for clamped-free Euler–Bernoulli beam.

displacements, is identically zero for all t. The generalized coordinates $p_k^j(t)$ are expressed in terms of harmonic functions. The elastic rotations $\varphi_k^1(\eta;t)$ and $\varphi_k^3(\eta;t)$ are obtained by evaluating the partial derivative of the displacement's components, $u_k^1(\eta;t)$ and $u_k^3(\eta;t)$, with respect to η, respectively. Moreover, the rotation $\varphi_k^2(\eta;t)$ is interpolated by a linear function and this rotation represents the twist angle around the elastic axis; that is,

$$\begin{aligned}\varphi_k^1(\eta;t) &= \partial_\eta u_k^3(\eta;t) = d_\eta(H_k^3(\eta))p_k^3(t)\\ \varphi_k^2(\eta;t) &= H_k^{\text{twist}}(\eta)p_k^{\text{twist}}(t) = \frac{\eta}{R}p_k^{\text{twist}}(t) \quad \text{and}\\ \varphi_k^3(\eta;t) &= -\partial_\eta u_k^1(\eta;t) = -d_\eta(H_k^1(\eta))p_k^1(t)\end{aligned} \tag{10}$$

where ∂_η denotes partial derivative with respect to η, d_η denotes total derivative with respect to η, $p_k^{\text{twist}}(t)$ is the generalized elastic coordinate that regulates the time variation of the wing torsion, and R is the wing length.

This formulation allows rewriting the elastic displacement vector of an arbitrary point P on the wing as

$$\mathbf{u}_k = \mathbf{u}_k^{P'} - \bar{\mathbf{s}}_k^{P'P}\boldsymbol{\varphi}_k = \mathbf{N}_k\mathbf{p}_k, \quad \text{for } k = 2,3 \tag{11}$$

where

$$\mathbf{N}_k = \begin{bmatrix} H_k^1 + s_k^2 d_\eta(H_k^1) & s_k^3 H_k^{\text{twist}} & 0\\ -s_k^1 d_\eta(H_k^1) & 0 & -s_k^3 d_\eta(H_k^3)\\ 0 & -s_k^1 H_k^{\text{twist}} & s_k^2 d_\eta(H_k^3) + H_k^3 \end{bmatrix} \quad \text{and}$$
$$\mathbf{p}_k = (p_k^1(t), p_k^{\text{twist}}(t), p_k^3(t))^T \tag{12}$$

$\mathbf{N}_k$ is a form of shape function matrix and $\mathbf{p}_k$ is an array containing the elastic generalized coordinates.

D. Equations of Motion

Once the absolute vector of translational velocity for any point on the body is known, the equations of motion can be derived. Additionally, it is important to consider that a flexible body can be constrained [45,47,48], by either linking it with other bodies or by choosing the parameters to describe primary motions. Only holonomic constraints are considered. The constrained Lagrange's equations are given by

$$d_t(\partial_{\dot{\mathbf{q}}_k} T_k) - \partial_{\mathbf{q}_k} T_k + \mathbf{B}_{\mathbf{q}_k}^T \boldsymbol{\lambda}_k = \mathbf{Q}_k^T \tag{13}$$

which are complemented by a set of algebraic-constraint equations expressed as

$$\boldsymbol{\Phi}_k(\mathbf{q}_{k-1}, \mathbf{q}_k, \mathbf{q}_{k+1}; t) = 0 \tag{14}$$

where $\mathbf{q}_k$ is as defined previously, and d_t, $\partial_{\mathbf{q}_k}$, and $\partial_{\dot{\mathbf{q}}_k}$ denote the first temporal derivative, the partial derivative with respect to $\mathbf{q}_k$, and the partial derivative with respect to $\dot{\mathbf{q}}_k$, respectively. $\boldsymbol{\lambda}_k$ is the vector of Lagrange's multipliers for the kth body, $\mathbf{B}_{\mathbf{q}_k}$ is the Jacobian matrix of constraints associated to the set of coordinates $\mathbf{q}_k$, and $\mathbf{Q}_k$ is the generalized load vector comprising conservative and nonconservative loads.

The kinetic energy of the kth body is given by

$$T_k = \frac{1}{2}\int_{D_k} \rho_k(\dot{\boldsymbol{R}}_k^P \cdot \dot{\boldsymbol{R}}_k^P)\,\mathrm{d}D_k \quad \text{for } k = 1,2,3 \tag{15}$$

where ρ_k is the mass density per unit of volume, and dD_k is a kth body differential subdomain. For computing the kinetic energy, the authors use Eq. (6) for the central body and Eq. (7) for the wings.

1. *Equations for Wings*

Following the methodology proposed by Shabana [45], the angular velocity vector can be expressed as the product between a matrix $\mathbf{G}_k$ dependent of the particular parameterization of rotations chosen and a 3×1 array $\dot{\boldsymbol{\theta}}_k = (\dot{\phi}_k, \dot{\theta}_k, \dot{\psi}_k)^T$ whose components are the time derivative of the rotation parameters defined in Sec. III.A. Equation (7) can be used to describe the velocity of an arbitrary point on the left (right) wing. It can be rewritten in matrix notation as

$$\dot{\mathbf{R}}_k^P = [\,\mathbf{I}_3 | -\mathbf{Q}_{\text{NB}^k}(\bar{\mathbf{r}}_k + \bar{\mathbf{u}}_k)\mathbf{G}_k\,]\dot{\mathbf{q}}_k + \mathbf{Q}_{\text{NB}^k}\dot{\mathbf{u}}_k, \quad \text{for } k = 2,3 \tag{16}$$

where $\mathbf{I}_3$ is the 3×3 identity matrix and $\dot{\mathbf{q}}_k$ is the time derivative of the vector of absolute coordinates $\mathbf{q}_k$.

It is to be noted that $\dot{\mathbf{u}}_k$ is the time derivative of Eq. (11). On substituting Eq. (16) into Eq. (15), and performing algebraic manipulations, the kinetic energy for the kth body can be obtained as

Downloaded by UNIVERSITY OF MARYLAND on June 12, 2017 | http://arc.aiaa.org | DOI: 10.2514/1.J055137

$$T_k = \frac{1}{2}\dot{\mathbf{q}}_k^T \mathbf{M}_k \dot{\mathbf{q}}_k + \dot{\mathbf{p}}_k^T \mathfrak{M}_k \dot{\mathbf{q}}_k + \frac{1}{2}\dot{\mathbf{p}}_k^T \mathfrak{B}_k \dot{\mathbf{p}}_k, \quad \text{for } k = 2, 3 \tag{17}$$

where $\mathbf{M}_k$ is the mass matrix for primary motions, which is differentiable, symmetric, and at least positive semidefinite; $\mathfrak{M}_k$ is the mass matrix that couples primary and secondary motions; and $\mathfrak{B}_k$ is the mass matrix for secondary motions, which is constant, symmetric, and positive definite. These quantities can be expressed by means of submatrices as

$$\mathbf{M}_k = \left[\begin{array}{c|c} \mathbf{m}_k^{RR} & \mathbf{m}_k^{R\theta} \\ \hline \mathbf{m}_k^{\theta R} & \mathbf{m}_k^{\theta\theta} \end{array}\right], \quad \mathfrak{M}_k = \left[\begin{array}{c|c} \mathbf{m}_k^{PR} & \mathbf{m}_k^{P\theta} \end{array}\right], \quad \mathfrak{B}_k = \left[\mathbf{m}_k^{PP}\right], \tag{18}$$

where

$$\begin{aligned}
\mathbf{m}_k^{RR} &= m_k \mathbf{I}_3 \\
\mathbf{m}_k^{R\theta} &= -\mathbf{Q}_{\mathrm{NB}^k} \left\langle \int_{D_k} \rho_k (\bar{\mathbf{r}}_k + \bar{\mathbf{u}}_k)\, \mathrm{d}D_k \right\rangle \boldsymbol{G}_k \\
\mathbf{m}_k^{\theta\theta} &= \mathbf{G}_k^T \left\langle \int_{D_k} \rho_k (\bar{\mathbf{r}}_k + \bar{\mathbf{u}}_k)^T (\bar{\mathbf{r}}_k + \bar{\mathbf{u}}_k)\, \mathrm{d}D_k \right\rangle \boldsymbol{G}_k \\
\mathbf{m}_k^{PR} &= \left\langle \int_{D_k} \rho_k \mathbf{N}_k^T\, \mathrm{d}D_k \right\rangle \mathbf{Q}_{\mathrm{NB}^k}^T \\
\mathbf{m}_k^{P\theta} &= -\left\langle \int_{D_k} \rho_k \mathbf{N}_k^T (\bar{\mathbf{r}}_k + \bar{\mathbf{u}}_k)\, \mathrm{d}D_k \right\rangle \mathbf{G}_k \quad \text{and} \\
\mathbf{m}_k^{PP} &= \int_{D_k} \rho_k \mathbf{N}_k^T \mathbf{N}_k\, \mathrm{d}D_k
\end{aligned} \tag{19}$$

Finally, after making use of Eq. (17) in Lagrange's equations, the equations of motion for the kth body can be obtained as follows:

$$\begin{aligned}
&\mathbf{M}_k \ddot{\mathbf{q}}_k + \mathfrak{M}_k^T \ddot{\mathbf{p}}_k + \mathbf{B}_{\mathbf{q}_k}^T \boldsymbol{\lambda}_k = \mathbf{Q}_k^h + \mathbf{Q}_k^v + \mathbf{Q}_k^T, \quad \text{for } k = 2, 3 \\
&\boldsymbol{\Phi}_k = \mathbf{0}
\end{aligned} \tag{20}$$

where

$$\mathbf{Q}_k^v = -\dot{\mathbf{M}}_k \dot{\mathbf{q}}_k + \partial_{\mathbf{q}_k} (\dot{\mathbf{q}}_k^T \mathbf{M}_k \dot{\mathbf{q}}_k) \tag{21}$$

is a quadratic velocity vector obtained by differentiating a portion of the kinetic energy with respect to time and with respect to the set of coordinates $\mathbf{q}_k$ and accounts for gyroscopic effects from primary motions and

$$\mathbf{Q}_k^h = -\dot{\mathfrak{M}}_k \dot{\mathbf{p}}_k + \partial_{\mathbf{q}_k} (\dot{\mathbf{p}}_k^T \mathfrak{M}_k \dot{\mathbf{q}}_k) \tag{22}$$

results from imposition of deformations on the wings.

2. Equations for Central Body

The equations of motion for the central body are obtained by following the same procedure discussed in Sec. III.D.1. The only difference lies in the velocity vector expression. By using Eq. (6), the resulting kinetic energy expression for the central body is much simpler than that found for the wings; that is,

$$T_1 = \frac{1}{2}\dot{\mathbf{q}}_1^T \mathbf{M}_1 \dot{\mathbf{q}}_1 \tag{23}$$

where $\mathbf{M}_1$ is the mass matrix for the central body, which is differentiable, symmetric, and positive definite, and $\dot{\mathbf{q}}_1$ is the time derivative of the set of coordinates $\mathbf{q}_1$. By introducing Eq. (23) into Lagrange's equations, the equations of motion for the central body can be obtained as follows:

$$\mathbf{M}_1 \ddot{\mathbf{q}}_1 + \mathbf{B}_{\mathbf{q}_1}^T \boldsymbol{\lambda}_1 = \mathbf{Q}_1^v + \mathbf{Q}_1^T \quad \boldsymbol{\Phi}_1 = \mathbf{0} \tag{24}$$

where λ_1 is the set of Lagrange's multipliers for the central body, $\mathbf{B}_{\mathbf{q}_1}$ is the Jacobian matrix of constraints associated with the set of coordinates $\mathbf{q}_1$, $\mathbf{Q}_1$ is the vector of generalized conservative loads for the central body, and $\mathbf{Q}_1^v$ is a quadratic velocity vector, computed in the same way as $\mathbf{Q}_k^v$ [see Eq. (21)].

3. Equations of Motion for MAV

Finally, the equations of motion for the complete multibody system are obtained by assembling the equations of motion for each body (the wings and the central body); that is,

$$\mathbf{M}\ddot{\mathbf{q}} + \mathbf{B}_{\mathbf{q}}^T \boldsymbol{\lambda} = \mathbf{F} \quad \boldsymbol{\Phi} = 0 \tag{25}$$

where $\mathbf{M} \in \mathbb{R}^{n_{\mathrm{coord}} \times n_{\mathrm{coord}}}$ is the global mass matrix; $\mathbf{B}_{\mathbf{q}} \in \mathbb{R}^{n_c \times n_{\mathrm{coord}}}$ is the global constraint Jacobian matrix, $\mathbf{q} \in \mathbb{R}^{n_{\mathrm{coord}} \times 1}$ is the global vector of generalized coordinates, $\boldsymbol{\lambda} \in \mathbb{R}^{n_c \times 1}$ is the global vector of Lagrange's multipliers, $\mathbf{F} \in \mathbb{R}^{n_{\mathrm{coord}} \times 1}$ is the global vector of forces, in which all the contributions previously explained are collected, and $\boldsymbol{\Phi} \in \mathbb{R}^{n_c \times 1}$ is the set of all constraints for the multibody system.

E. Constraint Equations

For each wing, there are two different constraint equations: 1) position constraint, for specifying the connection point between a wing and the central body, and 2) orientation constraint, for specifying the orientation of each wing with respect to the central body.

To establish the connection between each wing and the central body, let us consider a frame $\mathbf{C}^k = \{{}^k\hat{\mathbf{c}}_1, {}^k\hat{\mathbf{c}}_2, {}^k\hat{\mathbf{c}}_3\}$ (for $k = 2, 3$) fixed at the point between a wing and the central body and oriented with respect to the reference frame $\mathbf{B}^1$ by means of specific kinematics. Then, the position and orientation of the reference frame $\mathbf{C}^k$ and the body-fixed frame attached to each wing $\mathbf{B}^k$ must be coincident; both the position and orientation are described by using different sets of generalized coordinates (see Fig. 3). To state that the orientation of both frames is coincident, the following three conditions must be satisfied: 1) the first element of the reference system of $\mathbf{C}^k$ must remain orthogonal to the second element of the reference system $\mathbf{B}^k$; 2) the second element of the reference system $\mathbf{C}^k$ must remain orthogonal to the third element of the reference system $\mathbf{B}^k$; and 3) the third element of reference system $\mathbf{C}^k$ must remain orthogonal to the first element of reference system $\mathbf{B}^k$. These conditions can be expressed as

$$\begin{aligned}
\phi_4 &= ({}^k\hat{\mathbf{b}}_1^T \mathbf{Q}_{\mathrm{NB}^k}^T)(\mathbf{Q}_{\mathrm{NC}^k}\, {}^k\hat{\mathbf{c}}_2) = 0 \\
\phi_5 &= ({}^k\hat{\mathbf{b}}_2^T \mathbf{Q}_{\mathrm{NB}^k}^T)(\mathbf{Q}_{\mathrm{NC}^k}\, {}^k\hat{\mathbf{c}}_3) = 0, \quad \text{and} \\
\phi_6 &= ({}^k\hat{\mathbf{b}}_3^T \mathbf{Q}_{\mathrm{NB}^k}^T)(\mathbf{Q}_{\mathrm{NC}^k}\, {}^k\mathbf{c}_1) = 0
\end{aligned} \tag{26}$$

where $\mathbf{Q}_{\mathrm{NC}^k}$ is the matrix representation of the rotation tensor $\boldsymbol{Q}_{\mathrm{NC}^k}: \mathbf{C}^k \to \mathbf{N}$, which is obtained by means of the composition $\boldsymbol{Q}_{\mathrm{NB}^1} \circ \boldsymbol{Q}_{B^1 C^k}$, and $\boldsymbol{Q}_{B^1 C^k}$ is a rotation tensor that exclusively depends

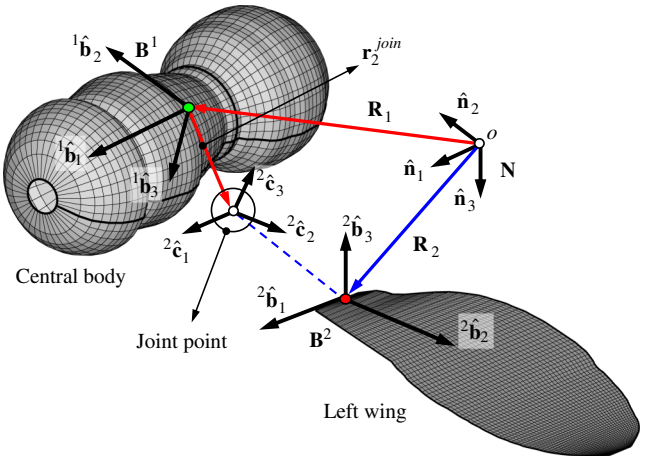

Fig. 3 Central body–left wing attachment.

Downloaded by UNIVERSITY OF MARYLAND on June 12, 2017 | http://arc.aiaa.org | DOI: 10.2514/1.J055137

on the adopted kinematics (for instance, the robofly kinematics or flapping animal kinematics) to describe the motion of each wing with respect to the central body.

Furthermore, to enforce that the position of the origins of both frames, $\mathbf{C}^k$ and $\mathbf{B}^k$, are the same, another three conditions must be satisfied. They establish that the difference between the components of the origin position vectors of both frames must be null and can be expressed as

$$\begin{aligned}\phi_1 &= \hat{\mathbf{n}}_1^T(\mathbf{R}_k - \boldsymbol{R}_1 - \mathbf{Q}_{\mathrm{NB}^1}\mathbf{r}_k^{\mathrm{join}}) = 0\\ \phi_2 &= \hat{\mathbf{n}}_2^T(\mathbf{R}_k - \mathbf{R}_1 - \mathbf{Q}_{\mathrm{NB}^1}\mathbf{r}_k^{\mathrm{join}}) = 0, \quad \text{and}\\ \phi_3 &= \hat{\mathbf{n}}_3^T(\mathbf{R}_k - \mathbf{R}_1 - \mathbf{Q}_{\mathrm{NB}^1}\mathbf{r}_k^{\mathrm{join}}) = 0\end{aligned} \tag{27}$$

where $\mathbf{r}_k^{\mathrm{join}}$ is the position vector of the joint for each wing relative to the origin of the reference frame $\mathbf{B}^1$ attached to the central body ($k = 2$ for the left wing and $k = 3$ for the right wing). Finally, by accounting the set of Eqs. (26) and (27), the authors write the vector of constraint equations for each wing as

$$\boldsymbol{\Phi}_k(\mathbf{q}; t) = (\phi_1, \phi_2, \phi_3, \phi_4, \phi_5, \phi_6)_k^T \tag{28}$$

F. Generalized Loads

The generalized loads associated with the set of absolute coordinates are determined by using the principle of virtual work [45,48]. These loads may be of very different nature. In this work, two kinds of forces are considered: 1) forces that result from aerodynamics (nonconservative) and 2) forces due to the action of the terrestrial gravitational field (conservative). The virtual work of an external force, $\boldsymbol{f}$, applied to the system can be expressed as

$$\overline{\delta W} = \boldsymbol{f} \cdot \delta \boldsymbol{r} \tag{29}$$

Where $\delta \boldsymbol{r}$ is an admissible virtual displacement contained in the tangent space $\mathcal{T}_r\mathcal{M}$ to the configuration space manifold $\mathcal{M}$ [49]. The virtual displacement of an arbitrary point belonging to the central body and each wing can be expressed as

$$\delta \boldsymbol{R}_1^P = \delta \boldsymbol{R}_1 + \delta(\boldsymbol{Q}_{\mathrm{NB}^1}\boldsymbol{r}_1), \quad \text{and} \tag{30}$$

$$\delta \boldsymbol{R}_k^P = \delta \boldsymbol{R}_k + \delta(\boldsymbol{Q}_{\mathrm{NB}^k}(\boldsymbol{r}_k + \boldsymbol{u}_k)), \quad \text{for } k = 2, 3 \tag{31}$$

As was stated previously, the wings can be considered rigid or undergo deformations following a determined pattern; then, the terms $\boldsymbol{r}_1$, $\boldsymbol{r}_k$, and $\boldsymbol{u}_k$ are independent of $\mathbf{q}_k$ for $k = 1, 2$, and 3, and therefore their variations are null.

By using Eq. (31) along with Eq. (29) and carrying out some manipulations, the following general expression for the aerodynamic generalized loads associated with each wing can be obtained:

$$\mathbf{Q}_k^{\mathrm{aero}} = \sum_{i=1}^{n_p} ({}^k\boldsymbol{f}_i^{\mathrm{aero}})^T(\mathbf{U} + \mathbf{V}_i), \quad \text{for } k = 2, 3 \tag{32}$$

Here, ${}^k\boldsymbol{f}_i^{\mathrm{aero}} = \Delta p_i^k A_i^k \hat{\boldsymbol{e}}_i^k$ [where Δp_i^k is the pressure jump computed with Eq. (1); $\hat{\boldsymbol{e}}_i^k$ is a unit vector at the control point of, and normal to, the ith aerodynamic element belonging to the kth body; and A_i^k is the area of the ith element belonging to the kth body]; $\mathbf{U} \in \mathbb{R}^{3\times 6}$ is a matrix whose components are $U_{\mathrm{rs}} = \delta_{\mathrm{rs}}$, where δ_{rs} is the Kronecker delta, n_p is the number of panels of the aerodynamic grid in each wing, and $\mathbf{V}_i \in \mathbb{R}^{3\times 6}$ is a matrix obtained from evaluating the partial derivative of $\mathbf{Q}_{\mathrm{NB}^k}(\mathbf{r}_k + \mathbf{u}_k)$ with respect to the vector of generalized coordinates $\mathbf{q}_k$.

By using Eq. (30), the generalized loads due to the terrestrial gravitational field are obtained with a similar procedure. Therefore, the mathematical expression for these terms is given by

$$\mathbf{Q}_1^{\mathrm{grav}} = \boldsymbol{f}_1^T\mathbf{I}_3 \quad \mathbf{Q}_k^{\mathrm{grav}} = \boldsymbol{f}_k^T(\mathbf{U} + \mathbf{V}_k), \quad \text{for } k = 2, 3 \tag{33}$$

where $\boldsymbol{f}_k = m_k g \hat{\mathbf{n}}_3$, m_k is the mass of the kth body, and g is the gravity acceleration constant. Finally, the load vector for the central body and each wing is expressed as

$$\mathbf{Q}_1 = \mathbf{Q}_1^{\mathrm{grav}}, \quad \text{and} \quad \mathbf{Q}_k = \mathbf{Q}_k^{\mathrm{grav}} + \mathbf{Q}_k^{\mathrm{aero}}, \quad \text{for } k = 2, 3 \tag{34}$$

It should be noted that the aerodynamic generalized loads are only due to the lifting surfaces (i.e., the wings). Although there is evidence that the insect's body contributes to the lift force, such phenomenon is not taken into account in this paper.

IV. Numerical Integration of the Index 1 DAEs

The set of equations of motion for the entire multibody system represents an index 3 system of DAEs. The index of a DAE is one *plus* the number of differentiations of the constraints that are needed in order to be able to eliminate the Lagrange multipliers λ. These dynamic equations are, in general, nonlinear. A closed-form solution for these equations is often difficult or even impossible to obtain. To solve them by means of standard solvers for ordinary differential equations (ODEs), an index reduction is required for the set of DAEs [48]. The methodology adopted in this work includes differentiation of the constraint equations twice with respect to time. This new set of equations is often called constraint acceleration level and is given by,

$$\ddot{\boldsymbol{\Phi}}(\mathbf{q}, \dot{\mathbf{q}}; t) = \mathbf{B}_{\mathbf{q}}\ddot{\mathbf{q}} + 2\partial_{\mathbf{q}}(\partial_t\boldsymbol{\Phi})\dot{\mathbf{q}} + \partial_{\mathrm{tt}}\boldsymbol{\Phi} + \partial_{\mathbf{q}}(\mathbf{B}_{\mathbf{q}}\dot{\mathbf{q}})\dot{\mathbf{q}} = 0 \tag{35}$$

where ∂_{tt} denotes the second partial time derivative. The equations of motion for the multibody system (25) can be re-written together with the acceleration level constraint equations, as an index 1 system of DAEs, meaning

$$\left[\begin{array}{c|c} \mathbf{M} & \mathbf{B}_{\mathbf{q}}^T \\ \hline \mathbf{B}_{\mathbf{q}} & \mathbf{0}_{12\times 18} \end{array}\right]\left\{\begin{array}{c} \ddot{\mathbf{q}} \\ \hline -\boldsymbol{\lambda} \end{array}\right\} = \left\{\begin{array}{c} \mathbf{F} \\ \hline -\boldsymbol{\kappa} \end{array}\right\}, \tag{36}$$

where $\boldsymbol{\kappa} = -2\partial_{\mathbf{q}}(\partial_t\boldsymbol{\Phi})\dot{\mathbf{q}} - \partial_{\mathrm{tt}}\boldsymbol{\Phi} - \partial_{\mathbf{q}}(\mathbf{B}_{\mathbf{q}}\dot{\mathbf{q}})\dot{\mathbf{q}}$.

The numerical integration of Eq. (36) is susceptible to instabilities as a consequence of truncation procedures and round-off errors. The most easily discernible instability is that the position and velocity constraints are no longer exactly satisfied; that is, a constraint drift occurs. Moreover, the drift magnitude and the error in generalized positions and velocities grow with time, in the worst case, quadratically. This is not because of the employed numerical method, but because the system is itself mildly unstable [50–53]. In the literature, several stabilization methods to correct this numerical drift can be found, among which the most widely used due to its simplicity is Baumgarte's technique [50,54]. However, this technique may not be sufficient in certain situations, and the choice of the parameters has proved to be difficult in practice. Another technique currently used to stabilize Eq. (36) is based on the projection of the solution onto the constraint manifold, or at least part of it. There are two basic ways to perform this projection: one of them consists of redefining the ODE by adding new Lagrange's multipliers, based on projected invariants, and the other approach consists of discretizing numerically the ODE, which at the end of each discretization step, the approximate solution, is projected onto the selected constraints manifold. This procedure is called coordinate projection [53]. In this work, the authors have adopted the coordinate projection method to control/eliminate the numerical drift that arises during the numerical integration of the index 1 DAEs.

A. Integration Scheme

The approach followed in this work treats the structural model (called Simulator 1) and the airflow model (called Simulator 2) as different subsystems of a single dynamical system. These two simulator engines exchange information bi-directionally in an iterative sequence in order to continuously improve the estimation of the structure's response and the aerodynamic loads, respectively. On

Downloaded by UNIVERSITY OF MARYLAND on June 12, 2017 | http://arc.aiaa.org | DOI: 10.2514/1.J055137

Downloaded by UNIVERSITY OF MARYLAND on June 12, 2017 | http://arc.aiaa.org | DOI: 10.2514/1.J055137

the one hand, the numerical scheme used by Simulator 2 is well known and can be found in texts such as [39,42]. On the other hand, the numerical procedure adopted for Simulator 1 to solve the equations of motion of the MAV is based on Hamming's fourth-order predictor-corrector method [39,55]. This scheme was chosen for two main reasons: 1) Simulator 2 behaves better when the loads are evaluated at integral time steps, and 2) aerodynamic loads contain contributions that are proportional to the accelerations (the so-called added-mass effects). These contributions come from the term $\partial_t \varphi$, where $\varphi(\boldsymbol{x}; t)$ is the velocity potential in Bernoulli's equation and it is proportional to the velocity. For both reasons, Runge–Kutta-type methods are not suitable for Simulator 1.

The set of second-order differential equations presented in Eq. (36) must be re-written as a first-order system to integrate equations in the time domain as follows:

1) At $t = 0$, the initial conditions are known.

2) At $t = \Delta t$, the solution is predicted by the explicit Euler method, and then corrected iteratively through the modified Euler method.

3) At $t = 2\Delta t$, the solution is predicted by the two-step Adams–Bashforth method, and then corrected iteratively with the two-step Adams–Moulton method.

4) At $t = 3\Delta t$, the solution is predicted by the three-step Adams–Bashforth method, and then corrected iteratively with the three-step Adams–Moulton method.

5) At $t = 4\Delta t$, $5\Delta t$, $6\Delta t$, ..., the solution is predicted and corrected by the fourth-order modified method of Hamming.

It is important to remark that Lagrange's multipliers are obtained at every time step as a part of the solution.

B. Co-Simulation Strategy

Recently, modern engineering applications are becoming difficult to solve because the modeling process is increasingly complex. The common practice to solve such large systems is to perform a decomposition and use specific solvers for each partition (while continuously updating in each the information of the other) and iterating until numerical convergence is reached. In the context of this paper, *simulation* refers to a numerical solution of a continuous system, whereas *co-simulation* describes the concept of simultaneous executions of multiple interacting subsystem simulators [36]. During a time step Δt, the wakes are consistently convected to their new positions with the requirement that vorticity moves with the fluid particles, while, simultaneously, the structure of the MAV moves to their new position as a result of the acting forces and constraint equations. This concept is implemented by performing the following sequence of steps to calculate the solution at time $t + \Delta t$ as follows:

1) Simulator 2 is used to convect the wakes to their new positions. A fluid particle in the wake moves from its current position $\boldsymbol{x}(t)$ to its new position $\boldsymbol{x}(t + \Delta t)$ according to Eq. (2). During the rest of the procedure for this time step, the wake is frozen.

2) Simulator 1 uses the current loads computed by Simulator 2 to predict the response of the MAV structure.

3) The current state of the MAV is used as input of Simulator 2 and the loads are recalculated, but as stated above, the wake remains frozen. Then, these loads are used as input of Simulator 1 and the state of the MAV is updated. This step is repeated until convergence. Usually, three to seven iterations are required to reduce the error to be less than 10^{-10}.

4) Then, the final position and velocity of the MAV are evaluated by Simulator 1, and these values are used by Simulator 2 to recalculate the flow field and obtain the final estimate for the aerodynamic loads.

The procedure described above needs information from four previous time steps. At the beginning of the procedure, this information does not exist, and so the authors have used a special starting scheme: at $t = 0$, the initial conditions are used by Simulator 2 to calculate the aerodynamic loads ignoring the contribution of $\partial_t \varphi$. Mostly, it is not important to capture this contribution accurately at this step because the response of the structure is being determined for an arbitrary initial disturbance. However, further studies on this issue are needed to definitively state that $\partial_t \varphi$ can be neglected at $t = 0$.

Although Simulator 1 and Simulator 2 are computational implementations of physical fields independently modeled as the aerodynamics and the MAV structure, the coupling procedure is indeed strong because information is bidirectionally exchanged, and the chosen step, which advances the solution in time, is unique for both simulation environments. In Fig. 4, a detailed flowchart for the proposed aerodynamics-structural dynamics co-simulation framework is presented.

C. Stabilization Scheme

A technique based on the coordinate projection is used in this work in order to control/eliminate the numerical drift that arises from the integration of Eq. (36). This approach consists in discretizing numerically the index 1 DAEs, computing the solution at t_{n+1} by means of Hamming's scheme, and then, at the end of each discretization step, projecting the approximate solution onto the constraints manifold. It is possible to choose three different ways to project the approximate solution: 1) onto the position constraints manifold, 2) onto the velocity constraints manifold, or 3) onto both, which may be more expensive. Such a projection is performed as

$$\mathbf{z}_{n+1} = \tilde{\mathbf{z}}_{n+1} - \gamma \mathbf{L}(\tilde{\mathbf{z}}_{n+1}; t_{n+1}) \mathbf{h}(\tilde{\mathbf{z}}_{n+1}; t_{n+1}) \tag{37}$$

where $\mathbf{z}_{n+1} = (\mathbf{q}_{n+1}, \dot{\mathbf{q}}_{n+1})$, $\tilde{\mathbf{z}}_{n+1}$ is the solution computed from the Hamming's method at $t = t_{n+1}$, and $\mathbf{h}(\tilde{\mathbf{z}}_{n+1}; t_{n+1})$ form an invariant set of the index 1 DAEs, which depend on the selected constraints manifold to project the solution [51–53] and is given by the following expression

$$\mathbf{h}(\mathbf{z}; t) = \begin{Bmatrix} \Phi(\mathbf{q}; t) \\ \mathbf{B}_\mathbf{q} \dot{\mathbf{q}} + \partial_t \Phi(\mathbf{q}; t) \end{Bmatrix} = 0 \tag{38}$$

The stabilization scheme (37) shows the desired stability behavior if $\mathbf{CL}$ is positive definite, with $\mathbf{C} = \partial_\mathbf{z} \mathbf{h}$ and $\mathbf{L}$ being the stabilization matrix. For most mechanical systems in engineering, the projection scheme (37) results asymptotically stable for $0 < \gamma < 2$, and for the choice $\gamma = 1$, which certainly depends on the discretization step size Δt is close to be optimal. Computation of the stabilization matrix $\mathbf{L}$ is generally a complex process, and to ensure poststabilization effectiveness, one must design $\mathbf{L}$ so that $\|\mathbf{I} - \mathbf{CL}\| < 1$ [56]. Three possible choices for $\mathbf{L}$ widely used in multibody dynamics are as follows:

$$\mathbf{L} = \mathbf{B}_\mathbf{q}^T (\mathbf{B}_\mathbf{q} \mathbf{B}_\mathbf{q}^T)^{-1} \begin{bmatrix} \boldsymbol{I}_{n_c} & 0 \\ -\langle \partial_\mathbf{q} (\mathbf{B}_\mathbf{q} \dot{\mathbf{q}}) + \partial_\mathbf{q} (\partial_t \Phi) \rangle \mathbf{B}_\mathbf{q}^T (\mathbf{B}_\mathbf{q} \mathbf{B}_\mathbf{q}^T)^{-1} & \mathbf{I}_{n_c} \end{bmatrix} \tag{39}$$

$$\mathbf{L} = \mathbf{B}_\mathbf{q}^T (\mathbf{B}_\mathbf{q} \mathbf{M}^{-1} \mathbf{B}_\mathbf{q}^T)^{-1} \begin{bmatrix} \mathbf{I}_{n_c} & 0 \\ 0 & \mathbf{I}_{n_c} \end{bmatrix} \tag{40}$$

$$\mathbf{L} = \mathbf{B}_\mathbf{q}^T (\mathbf{B}_\mathbf{q} \mathbf{B}_\mathbf{q}^T)^{-1} \begin{bmatrix} \mathbf{I}_{n_c} & 0 \\ 0 & \mathbf{I}_{n_c} \end{bmatrix} \tag{41}$$

where $\mathbf{I}_{n_c}$ is the $n_c \times n_c$ identity matrix, and $\mathbf{0}$ is the $n_c \times n_c$ null matrix. More details about the selection criteria for matrix $\mathbf{L}$ can be found in [52,53]. The definitions presented above for matrix $\mathbf{L}$ help generate different poststabilization schemes, successfully implemented in this work. These schemes are listed next:

1) *S-full*: using the stabilization scheme (38) with projection on both velocity and position levels using the $\mathbf{L}$ matrix defined in Eq. (39).

2) *S-both*: using the stabilization scheme (38) with projection on both velocity and position levels using the $\mathbf{L}$ matrix defined in Eq. (41).

Downloaded by UNIVERSITY OF MARYLAND on June 12, 2017 | http://arc.aiaa.org | DOI: 10.2514/1.J055137

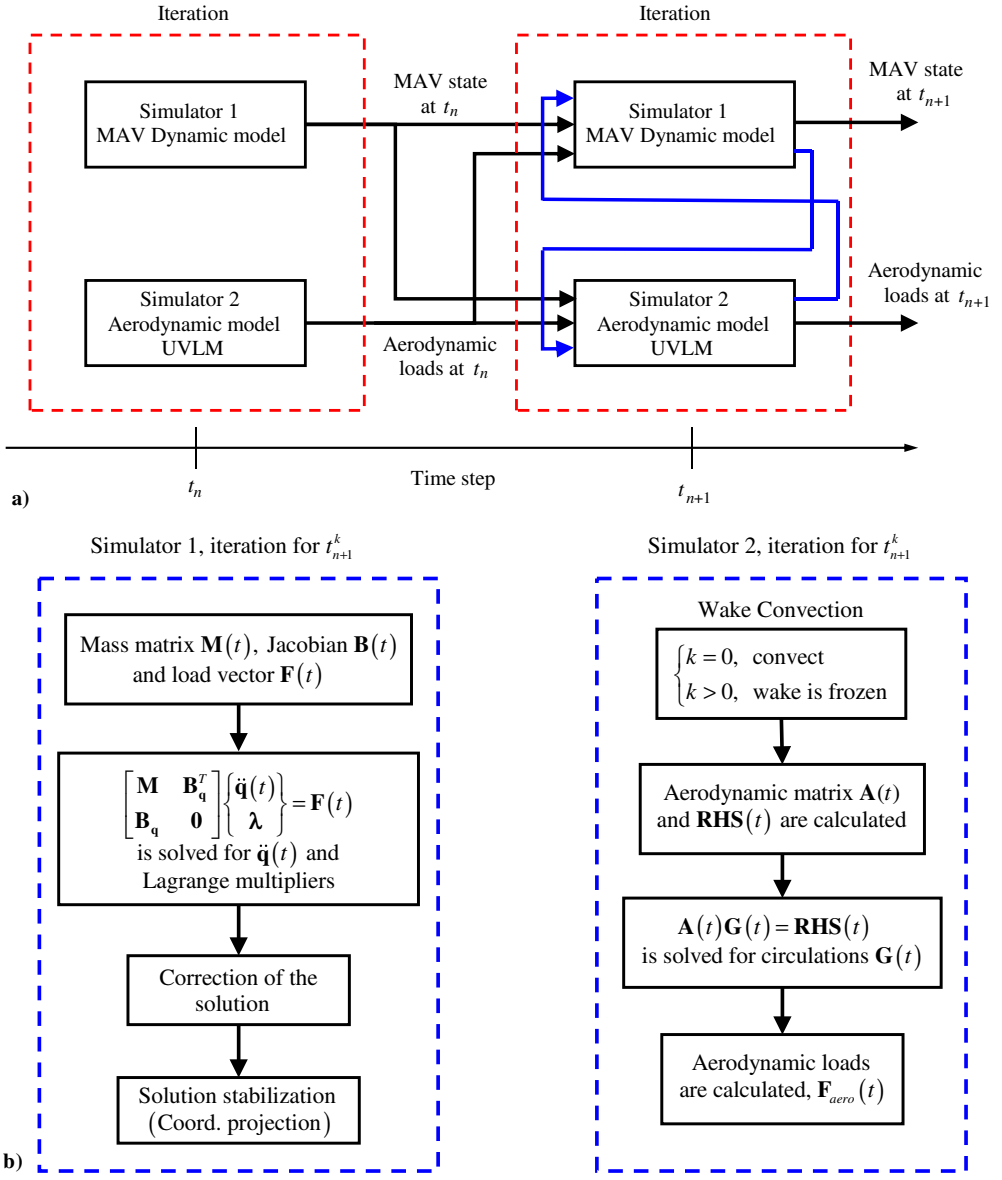

Fig. 4 Co-simulation framework: a) coupling scheme between Simulator 1 and Simulator 2, and b) flowcharts for Simulator 1 and Simulator 2.

3) *S-both-m*: using the stabilization scheme (38) with projection on both velocity and position levels using the **L** matrix defined in Eq. (40).

4) *S-pos*: using the stabilization scheme (38) with projection only on position level constraint using the **L** matrix defined in Eq. (41).

5) *S-vel*: using the stabilization scheme (38) with projection only on velocity level constraint using the **L** matrix defined in Eq. (41).

It should be mentioned that the *S-full* scheme is not commonly used because it is expensive. Instead, the same degree of precision can be obtained by applying the *S-both* scheme twice, denoted commonly in the literature as *S-both*^{2}. An algorithm for implementing *S-both*^{2} can be found in [56].

Finally, another issue to mitigate constraint violations is to start an integration process with a set of initial conditions on the coordinates and velocities that satisfy their corresponding constraints. To find an adequate set of initial conditions, the authors used the procedure described by Nikravesh [57], which is based on a partition of coordinates and velocities into dependent and independent sets. It is important to mention that this method does not consider any correction in the estimated values of the independent variables. Therefore, the kinematics constraints at coordinate and velocity levels are restated as

$$\mathbf{\Phi}(\mathbf{q}_{\text{ind}}, \mathbf{q}_{\text{dep}}; t) = 0 \tag{42}$$

and

$$\begin{bmatrix} \mathbf{B}_{\mathbf{q}_{\text{dep}}} & \mathbf{B}_{\mathbf{q}_{\text{ind}}} \\ 0 & \mathbf{I}_{\text{DOF}} \end{bmatrix} \begin{Bmatrix} \dot{\mathbf{q}}_{\text{dep}} \\ \dot{\mathbf{q}}_{\text{ind}} \end{Bmatrix} = \begin{Bmatrix} -\partial_t \mathbf{\Phi} \\ \dot{\mathbf{q}}_{\text{ind}} \end{Bmatrix} \tag{43}$$

where ind stands for independent coordinates; dep stands for dependent coordinates; $\mathbf{B}_{\mathbf{q}_{\text{dep}}}$ is selected to be a nonsingular matrix, with dimension $n_c \times n_c$; $\mathbf{B}_{\mathbf{q}_{\text{ind}}}$ is a matrix, with dimension $n_c \times n_{\text{DOF}}$; and $\mathbf{I}_{\text{DOF}}$ represents an identity matrix, with dimension $n_{\text{DOF}} \times n_{\text{DOF}}$.

The equation set (42) is solved iteratively by the Newton–Raphson method, and set (43) is solved as a set of linear algebraic equations.

V. Numerical Results

In this section, results obtained from the implementation of the proposed methodology written in Fortran 90 are presented. This implementation is highly structured in a modular organization; that is, each component can be individually removed and replaced, as well as the capability of adding new models without modifying the general structure of the program. Automatic optimization options, which are specific for Intel processors, have been used to improve performance. For all cases, the code was run on a desktop computer with an i7 processor, RAM DDR3 of 8 GB, and a hard disk of 2 TB.

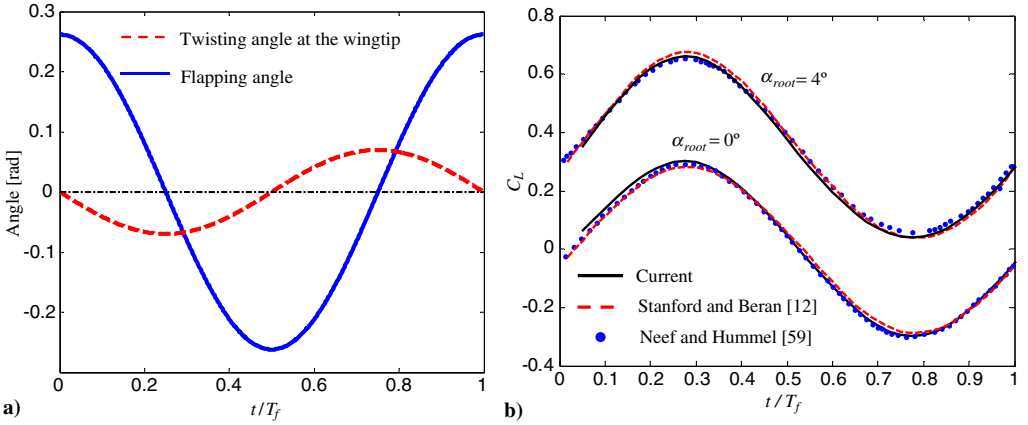

Fig. 5 a) Flapping and twisting motions used by Neef and Hummel [59] and b) comparison of lift coefficient obtained from current study with previous numerical results.

Downloaded by UNIVERSITY OF MARYLAND on June 12, 2017 | http://arc.aiaa.org | DOI: 10.2514/1.J055137

The results obtained by using the current numerical tool are compared against other published numerical results and experimental data to assess the validity and limitations of the present code. The aerodynamic model used in this work was previously validated by Roccia et al. [16]. Some of these validations are incorporated here for convenience. Then, the stability of the numerical integration scheme is validated and so is the dynamic model by means of comparing numerical results with analytical formulas. Finally, the aerodynamics and dynamics of a fruit fly are analyzed in free hover flight. As part of this study, specific deformation patterns on the wings are applied in order to evaluate their influence on the aerodynamic performance. Finally, to validate the quality of the numerical results, the authors have compared the aerodynamic loads obtained from the numerical simulations with experimental force data published by Fry et al. [58].

A. Validation of Model for Aerodynamics

1. *Flapping/Twisting Wing*

Neef and Hummel [59] considered a rectangular wing of $AR = 8$, a NACA 0012 profile, a flapping amplitude of 15°, and a reduced frequency $k = 0.1$ (k is defined as $n_f c/2V_\infty$, where n_f is the flapping frequency, c is the wing chord, and V_∞ is the free-stream velocity magnitude). The flapping motion is sinusoidal, and an out-of-phase wing rotation, twist, around the leading edge is imposed linearly along the span, with 4° of twist at the tip. The flapping period T_f was discretized into 40 equal time steps. In Fig. 5a, the kinematic pattern is provided. Two sets of comparative results of the lift coefficient for a flapping/twisting wing with its root chord inclined at two constant angles of attack (α_{root}) of 0° and 4° are presented in Fig. 5b. The results of Neef and Hummel [59] were computed by solving the Euler equations, and the results of Stanford and Beran [12] by using their own version of the UVLM. It is observed that the agreement among the three sets of results is excellent. The minor differences between the lift force computed by Stanford and Beran and the one calculated in this work lie in the specification of some user-defined parameters, such as the cutoff radius and differences in the two versions of Bernoulli's equation. In the current numerical experiment, the wing–tip vortex system has been omitted.

2. *Hovering Wing*

In this sub-subsection, the lift forces obtained from numerical simulations are presented and compared with the experimental data reported by Dickinson et al. [40]. The experiment carried out by Dickinson and co-workers consists of a dynamically scaled model of a *Drosophila melanogaster*, called the *Robofly*. The motions of the two wings are driven by an assembly of six computer-controlled stepper motors, and each wing is capable of rotational motions about three axes. The wings are immersed in a one-by-two-meter cross-section tank filled with mineral oil with density $\rho = 880$ kg/m^3 and kinematic viscosity $\nu = 115cSt$. The wings perform an insect-like flapping motion at a frequency of 0.145 Hz and the wing tips trace out a flat figure of eight. The kinematic pattern employed in this earlier work is characterized by a stroke amplitude of 160° and an angle of attack at midstroke equal to 40°, for both the upstroke and downstroke. A comparison of the lift force obtained using the aerodynamic simulation framework and the experimental results published by Dickinson et al. [40] is presented in Fig. 6, for three different phase relations between wing rotation and the reversal stroke: 1) wing rotation precedes the reversal stroke by 8% of the wing–beat cycle; 2) wing rotation occurs symmetrically with respect to the reversal stroke; 3) wing rotation is delayed with respect to the stroke reversal by 8% of the stroke cycle.

The numerical results obtained applying the proposed approach are encouraging, because they show better agreement than those reported in previously published comparisons; for instance, the CFD study by Sun and Tang [7], which shows relatively poor agreement with the experimental data from Dickinson et al. [40], and the 2D aerodynamic model developed by Ansari et al. [60,61], which shows similar trends for lift and thrust forces, but the magnitude of positive and negative spikes for lift and thrust, overestimates the experimental measures reported by Birch and Dickinson [62]. The current results are significant because they justify the use of the nonlinear UVLM to characterize 3D aerodynamic behavior of insects executing different maneuvers. For a detailed validation of this aerodynamic simulation framework by using a modified version of the UVLM applied to flapping wings, the reader can consult the work of Roccia et al. [16].

B. Validation of Model for Dynamics

To validate the numerical integration scheme and the current model for vehicle dynamics, a simplified version of the problem is considered in which the aerodynamic loads on the insect's wing are suppressed leaving it in a free fall. Data reported by Bos et al. [63] about the kinematics of a fruit fly (*D. melanogaster*) in hover flight are used to describe the pattern of wing motion over a flapping cycle. The setup for the numerical experiment shown in this subsection has the following parameters: 1) a flapping frequency $n_f = 200$ Hz and 2) an integration step size $= \Delta t = 0.01$ units.

In Table 1, the authors show the magnitude of the constraint violations (numerical drifts) based on runs done by using the four-order Hamming method with a constant step size. Numerical simulations for three flapping cycles were carried out by implementing the following coordinate-projection schemes: *S-full*, *S-both*, *S-both*^{2}, *S-pos*, *S-vel*, and *S-both-m*, respectively. It can be observed that the stabilization at the position level, when *S-pos*, *S-both*, and *S-both*^{2} are used, yields good results, whereas *S-pos* and *S-both* stabilizations do not yield good results for the velocity level. Of all these variants, the stabilization *S-both*^{2} is preferred because it produces the best results on both position and velocity levels.

In addition, other stabilization procedures, such as Baumgarte method, were tested, but all these techniques showed a significant numerical drift in the orientation constraints at the position level. The poor capability of Baumgarte method to adequately control the numerical drift associated with the orientation constraints is possibly due

Downloaded by UNIVERSITY OF MARYLAND on June 12, 2017 | http://arc.aiaa.org | DOI: 10.2514/1.J055137

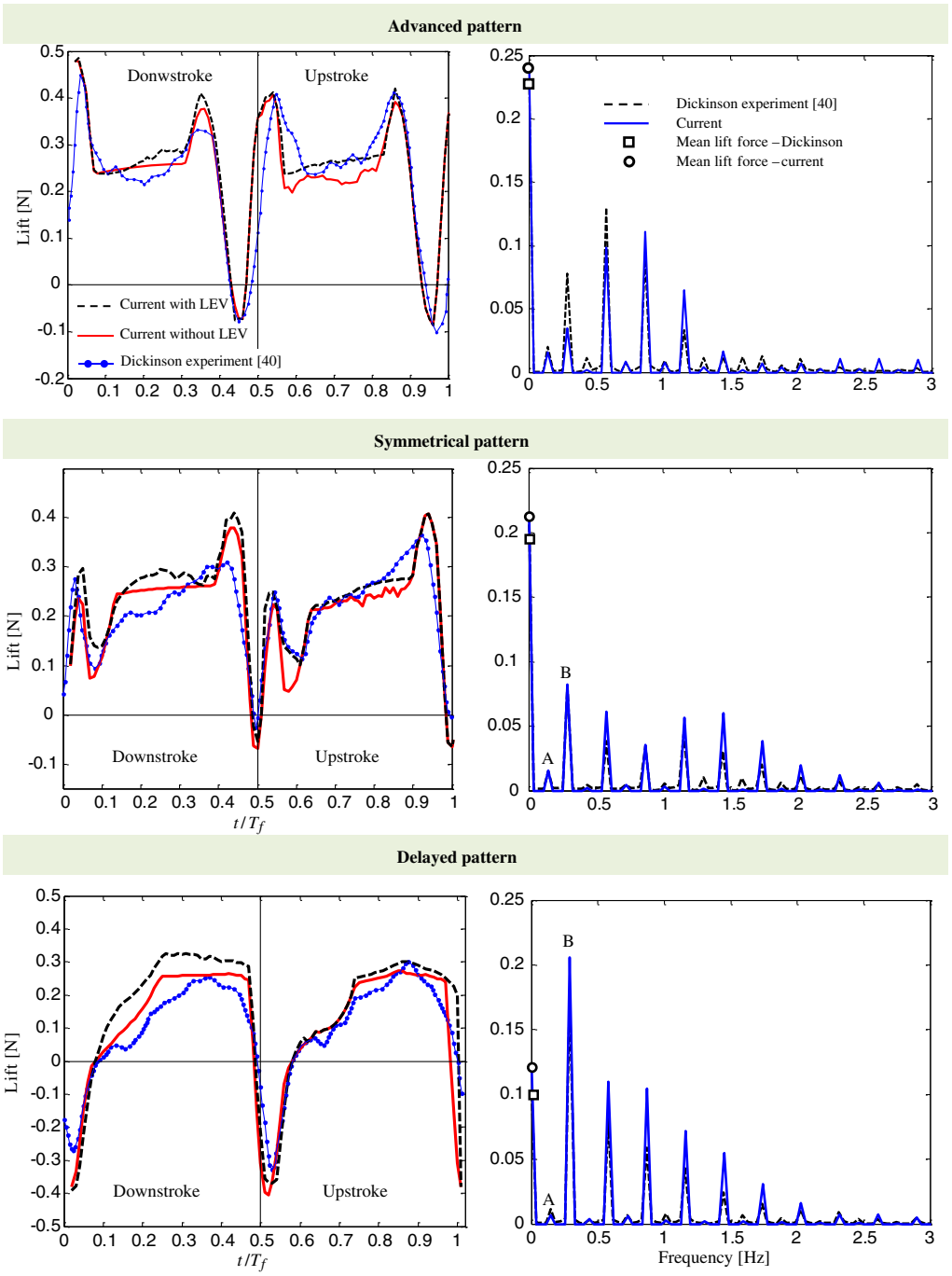

Fig. 6 Comparison of numerical results and experimental measurements for the Robofly apparatus (first stroke cycle) [16].

to a number of factors, among which the following are highlighted: 1) the step size adopted, which finally depends on the aerodynamic discretization, 2) the heterogeneity of the aeronautical system (rate $m_{\text{central body}}/m_{\text{wing}} \approx 200$), and 3) the complexity of the orientation constraint equations, which explicitly depend on time.

To finally validate the dynamic model presented in Sec. III, the authors compare the vertical coordinate of the center of mass of the MAV against the formula $1/2gt^2$. As before, the aerodynamic loads were suppressed and two cases of study are considered: 1) the wings remain fixed to the central body, and 2) the wings have a prescribed

Table 1 Numerical drift for different coordinate projection schemes

	Drift position		Drift velocity	
Stabilization	Connection constraint	Orientation constraint	Connection constraint	Orientation constraint
S-full	6.0×10^{-7}	1.5×10^{-5}	4.0×10^{-7}	3.0×10^{-4}
S-both	6.0×10^{-10}	1.5×10^{-8}	2.0×10^{-7}	5.0×10^{-4}
S-both^2	2.0×10^{-16}	9.0×10^{-9}	1.0×10^{-11}	9.0×10^{-8}
S-pos	6.0×10^{-10}	1.0×10^{-8}	7.0×10^{-8}	8.0×10^{-3}
S-vel	1.5×10^{-9}	1.0×10^{-4}	4.0×10^{-17}	4.0×10^{-15}
S-both-m	6.0×10^{-8}	1.0×10^{-3}	5.0×10^{-7}	4.0×10^{-2}

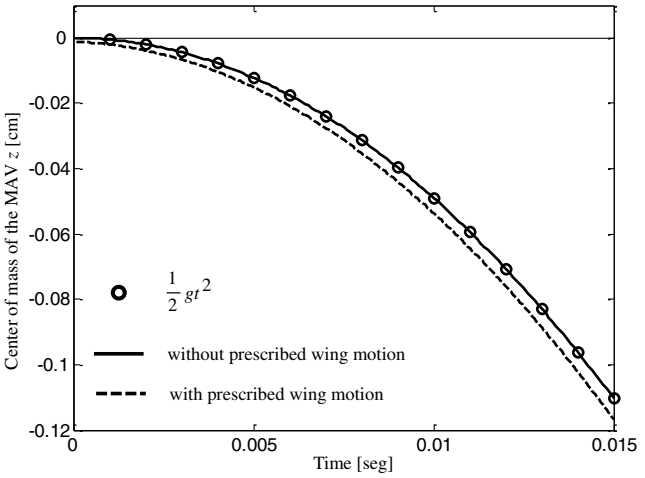

Fig. 7 Vertical coordinate of the MAV's mass center versus time.

motion with respect to the central body. Numerical simulations were carried out for three flapping cycle (300 time steps with $\Delta t = 0.01$). It should be noted that the variable Δt is dimensionless and each flapping cycle is discretized in 100 steps.

From Fig. 7, it is clear that the vertical coordinate predicted by the current model for dynamics of the MAV in free fall without prescribed wing motion coincides exactly with the results obtained by the simple formula $1/2gt^2$. Moreover, whether a prescribed motion is added, small differences from the previous curves are observed. This is because the initial velocity associated with the wings is the initial velocity of the whole mechanical system (in this case downward).

C. Computational Dynamics of MAV-Like Flapping Wings

In this sub-subsection, numerical results are presented for the aerodynamic and dynamic behavior of a flapping-wing MAV (fruit fly) in hovering flight. Data reported by Fry et al. [58] on the kinematics of a fruit fly in hover are used to describe the pattern of wing motion over a flapping cycle with respect to the central body, as presented in Fig. 8. Because of the complex motions the wings undergo during a stroke cycle due to the real kinematics (a slightly deformed eight pattern), the wake shed from the leading edge during the downstroke is cut by the wing when it moves in the opposite direction (upstroke). The wake rupture model is not yet available, and therefore, for consistency, the leading-edge separation model was deactivated.

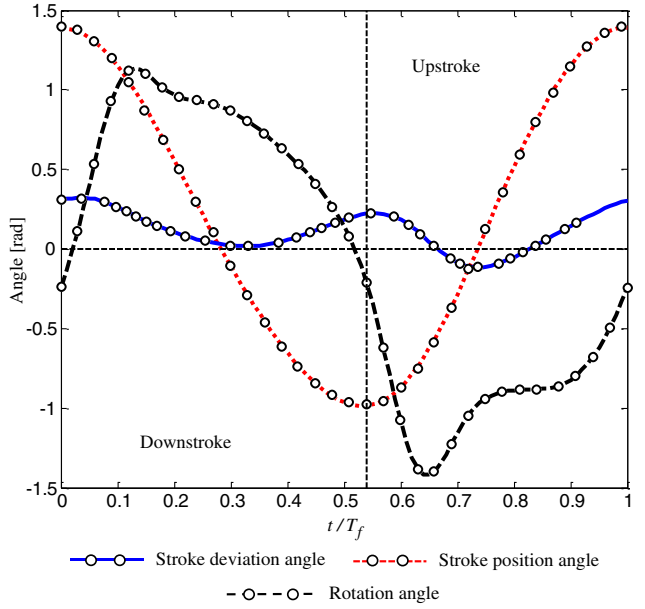

Fig. 8 Actual kinematics of a fruit fly in hovering. Circular markers represent experimental data.

According to observations performed by Ellington [64] and Ennos [65] on the wing kinematics of hoverflies, involving quantitative measurements of wing–tip paths and qualitative descriptions of wing deformation, twist is increased from zero to some constant value at the beginning of either downstroke or upstroke and kept constant during the midportion of the half stroke. Near the end of the half stroke, twist decreases until it becomes zero at the end of the half stroke. They also detected that the geometric angle of attack varied approximately linearly along the wing span (termed *linear twist*). Walker et al. [66] showed that twist was approximately constant in the mid–half stroke, similar to that described by Ellington and Ennos. However, around the stroke reversal, the twist was much larger than at the mid–half stroke. On the basis of these observations, in the current study, the authors have assumed that the twist deformation varies linearly along the wing span. The temporal evolution of the spanwise twist through the stroke cycle can be approximately matched by using harmonic functions. The effect described in [66] on the reversal stroke might be partially modeled by changing the phase angle between the twist deformation and the wing motion.

Because of the lack of data on how flying insects bend their wings during the flapping cycle, the authors propose, as a first approach, to use eigenfunctions to prescribe the bending along the wing span (normal and tangential to the wing chord) and harmonic functions to account for the time variation during the stroke cycle.

Specifically, two cases are presented. In the first one, a rigid model of the wing is considered, and in the second one, a flexible wing is considered and a specific deformation pattern is imposed. Such a pattern is a combination of torsion and bending in the normal and tangential direction of the wing chord. The generalized coordinates $p_k^j(t)$ (recall $k = 2$ for left wing, and $k = 3$ for right wing), which describe the temporal bending and torsion variations, are specified by the following harmonic functions:

$$p_k^j(t) = a_k^j \sin(\omega_k^j t + \beta_k^j) \quad \text{for } j = 1, \ldots, 3 \tag{44}$$

where ω_k^j is the circular frequency, β_k^j is the phase angle between the temporal coordinate $p_k^j(t)$ and the stroke position angle previously defined, and a_k^j is the deformation amplitude associated with the wingtip.

The values specified in Table 2 for the three different deformation patterns are based on a detailed study carried out by the authors on the influence of spanwise twisting and bending on the lift force generation in flapping-wing MAVs [67]. To show the important role of wing flexibility in the production of lift, the parameters that regulate the deformation patterns were tuned in order to increase the lift force throughout the stroke cycle with respect to the rigid wing model. In this table, the acronym OPB means out-of-plane bending and IPB means in-plane bending. To simplify the shape function matrix $\mathbf{N}_k$ in Eq. (12), the authors have assumed that the wing surface (at the reference configuration) lies on the plane spanned by the unitary vectors ${}^k\hat{\mathbf{b}}_1$ and ${}^k\hat{\mathbf{b}}_2$, and by recalling that the cross section of the wing is assumed to be rigid and orthogonal to ${}^k\hat{\boldsymbol{b}}_2$, Eq. (12) for $\mathbf{N}_k$ is reduced to

$$\mathbf{N}_k = \begin{bmatrix} H_k^1 & 0 & 0 \\ -s_k^1 d_\eta(H_k^1) & 0 & 0 \\ 0 & -s_k^1 H_k^{\text{twist}} & H_k^3 \end{bmatrix} \tag{45}$$

The setup of the numerical experiments shown in this section is described by the following parameters: flapping frequency $n_f = 210$ Hz, wing length $R = 2.5$ mm, wing area $S = 2.21$ mm^2, air density $\rho_{\text{air}} = 1.2$ kg/m^3, MAV mass of 0.84 mg, and a fully spatial discretization of the MAV of 1405 aerodynamic panels. Two hundred panels are used to discretize each of the wings and 1005 panels are used to discretize the central body (the head, thorax, and abdomen of the insect). Only one stroke cycle is simulated (first), which is discretized in 100 time steps. The set of initial conditions for the two cases of study is body angle $= 75°$ and stroke plane angle $= 15°$. These values produce a horizontal stroke plane, which results in a hover flight configuration. Both the linear

Downloaded by UNIVERSITY OF MARYLAND on June 12, 2017 | http://arc.aiaa.org | DOI: 10.2514/1.J055137

Table 2 Deformation pattern configuration

Pattern	Phase angle β_k^j, rad	Circular frequency ω_k^j, rad/s	Amplitude, a_k^j	Description
Twisting (j = twist)	0.5π	$2\pi n_f$	10°	Advanced twisting pattern
OPB ($j = 3$)	0.5π	$2\pi n_f$	$0.1R$	Advanced OPB pattern
IPB ($j = 1$)	-0.5π	$2\pi n_f$	$0.1R$	Delayed IPB pattern

IPB, in-plane bending; OPB, out-of-plane bending.

velocity of the central body mass center and the angular velocity vector of such body are zero at $t = t_0$.

In Fig. 9, the authors show the lift and horizontal forces obtained numerically for both the rigid wing model and the flexible wing model, along with experimental measurements carried out by Fry et al. [58] for a fruit fly in hovering. The most important requirement of hovering flight is undoubtedly the value of the vertical force, which must efficiently compensate for the insect weight. In Fig. 9a, the peak force at the middle of each half stroke is shown, mainly during the upstroke. Specifically, the peak force produced by the flexible wing model is approximately 30% higher than that of the rigid wing model. This fact is also reflected in Fig. 10b, in which the degree of freedom associated with the vertical displacement of the mass center of the central body is plotted. When a rigid wing model is used, the lift force produced can hardly support the insect weight, showing a slight downward movement at the end of the stroke cycle. On the other hand, when a suitable deformation pattern is applied, not only is the lift generated sufficient to balance the insect weight, but also it rises almost continuously.

To validate the numerical simulations carried out in this section, the aerodynamic forces obtained numerically are compared with those obtained experimentally. As it can be observed in Fig. 9a, both rigid and flexible wings show a form and trend similar to those reported by Fry et al. [58]. Nevertheless, the lift levels predicted by the numerical models are lower than those obtained experimentally (approximately 14% lower for a flexible wing).

Possibly this fact is due to two factors: 1) LEV phenomenon is not taken into account and 2) the wing deformation is not exactly that exhibited by insects, but it is prescribed by means of harmonic functions. Regarding the horizontal force, which represents the induced drag, it presents differences much more marked than the lift force, compared with the results published by Fry et al. (see Fig. 9b). However, it should be noted that the aerodynamic model used is inviscid and therefore viscous effects are not captured. Furthermore, because the UVLM is based on thin airfoil theory, it does not account for the leading-edge suction [68], and only the normal component to the noncirculatory velocity is retained, that is, the contribution of pressure to the local lift. The contribution of the forces on the lattice elements to the induced drag/thrust is aligned with the instantaneous noncirculatory velocity, and it can be computed, for example, through the approximation proposed by Katz and Plotkin [69], by the analogy adopted from Sane [70], or by the method developed by Ehlers and Manro [71], in which the leading-edge suction is calculated in the same computation that is used to evaluate the pressure distribution due to the leading-edge vortex.

To accurately compute the thrust generated by the flapping motion of a planar wing, the contribution of the leading-edge suction force must be included in calculations, causing the resultant aerodynamic force vector to tilt toward the leading edge. Because this feature is not taken into account, the total thrust level is certainly underestimated. However, the shape and tendency of it is well captured, as seen from Fig. 9b. This figure is also illustrative of how the horizontal force is always opposite to the wing motion, leading to a longitudinal oscillation of the insect's body. This dynamic behavior can be noted from Fig. 10a. Unlike forward thrust and lift, sideways thrust (sideslip) cancels instantly due to the bilateral symmetry of the wing motion (see Fig. 10d.) Similarly, as each wing contributes to yaw and roll torque with opposite orientations, these moments sum to zero at each point in the stroke cycle, provided that the motion of the two wings is bilaterally symmetric; again, this can be discerned from Fig. 10d. On the contrary, the sign and magnitude of the pitch torque is the same for both wings, resulting in a strongly fluctuating time characteristic during the whole stroke cycle.

As can be noted from Fig. 10c, this fact directly affects the pitch angle. In the work of Fry et al. [58], it can be observed that the average pitch torque over a complete cycle is zero, and therefore the insect's body undergoes an oscillation in the pitch angle. In real insects, this phenomenon is controlled by the wing kinematics, the flapping frequency, and the precise motion of the head and abdomen relative to the insect's thorax [72,73]. Such a control mechanism is essential to prevent the pitch torque from growing indefinitely and eventually tumbling the insect. In this work, no control strategy has been applied, and therefore the pitch angle behaves very differently than expected. It decreases continuously for most of the flapping cycle, showing a slight increase toward the end of the upstroke phase (see Fig. 10c). If this behavior is extended to subsequent cycles, the insect would undoubtedly crash.

Downloaded by UNIVERSITY OF MARYLAND on June 12, 2017 | http://arc.aiaa.org | DOI: 10.2514/1.J055137

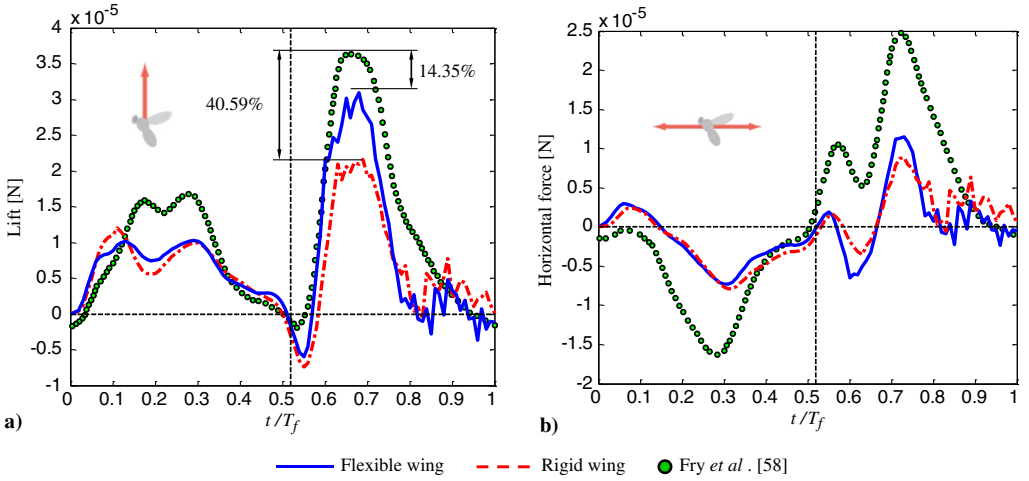

Fig. 9 Aerodynamic forces: a) lift component and b) horizontal component.

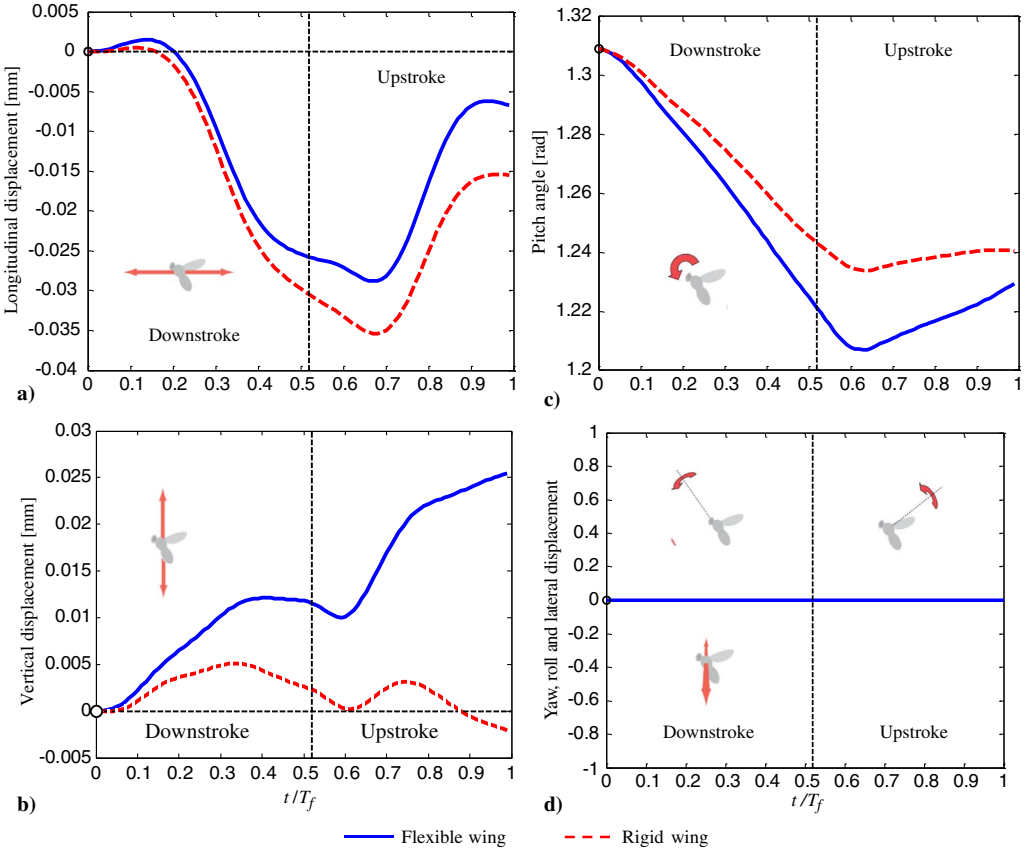

Fig. 10 Generalized coordinates of the central body: a) longitudinal displacement, b) vertical displacement, c) pitch angle, and d) roll, yaw, and lateral displacements.

D. Discussions and Future Improvements

Although the numerical results obtained with the present framework have been validated by using several well-known results in the literature, and the simulation results match experimental observations in the considered comparison cases, there are limitations with the current work that needs to be noted.

One of these limitations is that the aerodynamic model used is the result of an asymptotic approximation to the Navier–Stokes equations for a Reynolds number tending to infinity, which means that a model of the boundary layer is not included. During the computation of velocity using the Biot–Savart law, if the distance between a control point and a vortex segment was small enough, some problems may arise. This results in an unreasonably overestimated velocity, therefore resulting in unrealistic displacements of the aerodynamic nodes that define the vortex segments in the wakes. These numerical instabilities are much more significant in flight configurations, in which the wakes remain close and around an MAV's structure, hovering being an extreme condition, where the free-stream velocity is zero. Another significant limitation is that related to the common situation when a lifting surface cuts through its own wake; this issue is not addressed in this work, but it should definitely be considered in future studies.

As enhancements, the current aerodynamic model will be extended to describe wakes as collections of vortex particles. This will help improve the numerical treatment and smoothness characteristics of the wakes [14,74,75]. In addition, the use of the fast-multipole method to rapidly compute the velocity contribution from the time-varying wakes will also be very desirable [14,74,76]. Relative to the model for vehicle dynamics, one can conclude that the only significant limitation is related to the mechanism developed for prescribing deformation patterns on the considered MAV wings, which is valid only for small elastic displacements. Because of the importance of the elastic effects in the natural flight, the authors are working currently in a flexible wing model (by using a geometrically exact 3D beam; Cardona's beam model [77]) to carry out aeroelastic studies of flying insects as well as MAVs like flapping wings inspired by biology.

Despite the limitations outlined in the preceding paragraphs, the present computational dynamics framework is believed to be a credible alternative for studying flapping wings flight. Another feature that makes the current strategy attractive is the low computational cost compared with CFD simulations and/or finite element method–based approaches.

VI. Conclusions

In this paper, a co-simulation strategy for studying the dynamics and unsteady aerodynamics of flapping-wing micro-air-vehicles (MAVs) has been presented. The subsystem involving the dynamic model takes the inertial effects of the wings on the central body (fuselage) of the MAV into account and allow imposition of different deformation patterns on the wings such as torsion, bending in and out of the plane, and combinations of both. This dynamic model has also been successfully coupled in a strong way with the subsystem that models the aerodynamics, which is based on an expanded version of the unsteady vortex lattice method previously modified and validated by the authors of this paper. The numerical integration of the dynamical equations was performed successfully in the time domain by using a modified scheme proposed in this work. This modified scheme consists of the Hamming's fourth-order predictor-corrector method coupled with a poststabilization procedure based on the coordinate projection. The integration procedure as well as the vehicle dynamics model was validated by comparing the results with formula-based free fall results.

Some important inferences can be drawn from the preceding sections. The findings help to better understand the underlying physics associated with the unsteady aerodynamics and nonlinear dynamics of flapping wings, whose complexity is well-accepted but at the same time not usually well-understood. The numerical framework has been validated by comparing the numerical results with the data published by Fry et al. corresponding to a fruit fly in free

Downloaded by UNIVERSITY OF MARYLAND on June 12, 2017 | http://arc.aiaa.org | DOI: 10.2514/1.J055137

hovering flight. The lift force predicted for both the rigid wing model and the deformable wing model shows good agreement in terms of trends and experimental findings reported in the literature. However, it is acknowledged that the thrust magnitude was underestimated, possibly due to the noninclusion of the additional separation from the leading edge. Furthermore, the predicted horizontal force does have more marked differences from the experimental findings, and this is perhaps because the unsteady vortex-lattice method cannot account for viscous effects. However, the longitudinal coordinate shows a sort of oscillation in the horizontal direction, consistent with the experimental measurements.

Also, it should be noted that the imposition of suitable deformation patterns on the wings produces an increase in the lift force of 30% during upstroke, relative to the rigid wing model. This fact undoubtedly indicates that wing elasticity plays a fundamental role in the context of flapping-wing flight. This geometrical change in the wings, which does not necessarily match a real wing deformation pattern, is significant enough to produce the necessary lift increase to effectively compensate for the weight of the MAV and in turn to elevate it. Finally, a decrease, almost constant, in the value of the pitch angle for most of the beating cycles can be observed, which differs from the oscillatory feature reported in the literature. This observation points to the importance of control mechanisms to achieve a sustained and stable flight with flapping wings. These findings suggest the strong possibility that the aerodynamics–dynamics co-simulation strategy presented in this paper could play a role in decision-making systems designed for MAVs and other aircrafts.

Downloaded by UNIVERSITY OF MARYLAND on June 12, 2017 | http://arc.aiaa.org | DOI: 10.2514/1.J055137

Acknowledgments

The authors gratefully acknowledge the partial support received from the Consejo Nacional de Investigaciones Científicas y Técnicas, Argentina; the U.S. National Science Foundation through Grant No. CMMI-1250187; and the U.S. Air Force Office of Scientific Research through Grant No. FA95501510134. In addition, the authors would like to thank the Grupo de Electrónica Aplicada (GEA) and Grupo de Matemática Aplicada (GMA), Engineering School, Universidad Nacional de Río Cuarto, Argentina.

References

[1] Buckholz, R. H., "Measurements of Unsteady Periodic Forces Generated by the Blowfly Flying in a Wind Tunnel," *Journal of Experimental Biology*, Vol. 90, No. 1, 1981, pp. 163–173.

[2] Cloupeau, M., Devillers, J. F., and Devezeaux, D., "Direct Measurements of Instantaneous Lift in Desert Locust; Comparison with Jensen's Experiments on Detached Wings," *Journal of Experimental Biology*, Vol. 80, No. 1, 1979, pp. 1–15.

[3] Zanker, J. M., and Gotz, K. G., "The Wing Beat of Drosophila Melanogaster II. Dynamics," *Philosophical Transactions of the Royal Society of London, Series B: Biological Sciences*, Vol. 327, No. 1238, 1990, pp. 19–44. doi:10.1098/rstb.1990.0041

[4] Bennett, L., "Insect Flight: Lift and the Rate of Change of Incidence," *Science*, Vol. 167, No. 3915, 1970, 177–179. doi:10.1126/science.167.3915.177

[5] Isogai, K., Fujishiro, S., Saitoh, T., Yamamoto, M., Yamasaki, M., and Matsubara, M., "Unsteady Three-Dimensional Viscous Flow Simulation of a Dragonfly Hovering," *AIAA Journal*, Vol. 42, No. 10, 2004, pp. 2053–2059. doi:10.2514/1.6274

[6] Liu, H., Ellington, C. P., Kawachi, K., van den Berg, C., and Wilmott, A. P., "A Computational Fluid Dynamic Study of Hawkmoth Hovering," *Journal of Experimental Biology*, Vol. 201, No. 4, 1998, pp. 461–77.

[7] Sun, M., and Tang, J., "Unsteady Aerodynamic Force Generation by a Model Fruit Fly Wing in Flapping Motion," *Journal of Experimental Biology*, Vol. 205, No. 1, 2002, pp. 55–70.

[8] Ramamurti, R., and Sandberg, W. C., "A Three-Dimensional Computational Study of the Aerodynamic Mechanisms of Insect Flight," *Journal of Experimental Biology*, Vol. 205, No. 10, 2002, pp. 1507–1518.

[9] Kurtulus, D. F., Farcy, A., and Alemdaroglu, N., "Unsteady Aerodynamics of Flapping Airfoil in Hovering Flight at Low Reynolds Numbers," *43rd AIAA Aerospace Sciences Meeting and Exhibit*, AIAA Paper 2005-1356, 2005.

[10] Murua, J., Palacios, R., and Graham, J. M. R., "Applications of the Unsteady Vortex-Lattice Method in Aircraft Aeroelasticity and Flight Dynamics," *Progress in Aerospace Sciences*, Vol. 55, 2012, pp. 46–72. doi:10.1016/j.paerosci.2012.06.001

[11] Fritz, T. E., and Long, L. N., "Object-Oriented Unsteady Vortex Lattice Method for Flapping Flight," *Journal of Aircraft*, Vol. 41, No. 6, 2004, pp. 1275–1290. doi:10.2514/1.7357

[12] Stanford, B. K., and Beran, P. S., "Analytical Sensitivity Analysis of an Unsteady Vortex-Lattice Method for Flapping-Wing Optimization," *Journal of Aircraft*, Vol. 47, No. 2, 2010, pp. 647–662. doi:10.2514/1.46259

[13] Ghommem, M., Hajj, M. R., Mook, D. T., Stanford, B. K., Beran, P. S., Snyder, R. D., and Watson, L. T., "Global Optimization of Actively Morphing Flapping Wings," *Journal of Fluids and Structures*, Vol. 33, Aug. 2012, pp. 210–228. doi:10.1016/j.jfluidstructs.2012.04.013

[14] Willis, D. J., Peraire, J., and White, J. K., "A Combined pFFT-Miltipole Tree Code, Unsteady Panel Method with Vortex Particle Wakes," *International Journal of Numerical Methods in Fluids*, Vol. 53, No. 8, 2007, pp. 1399–1422. doi:10.1002/(ISSN)1097-0363

[15] Eldredge, J. D., "Numerical Simulation of the Fluid Dynamics of 2D Rigid Body Motion with the Vortex Particle Method," *Journal of Computational Physics*, Vol. 221, No. 2, 2007, pp. 626–648. doi:10.1016/j.jcp.2006.06.038

[16] Roccia, B. A., Preidikman, S., Massa, J. C., and Mook, D. T., "Modified Unsteady Vortex-Lattice Method to Study Flapping Wings in Hover Flight," *AIAA Journal*, Vol. 51, No. 11, 2013, pp. 2628–2642. doi:10.2514/1.J052262

[17] Taylor, G., and Thomas, A., "Dynamic Flight Stability in the Desert Locust Schistocera Gregaria," *Journal of Experimental Biology*, Vol. 206, No. 16, 2003, pp. 2803–2829. doi:10.1242/jeb.00501

[18] Sun, M., and Xiong, Y., "Dynamic Flight Stability of a Hovering Bumblebee," *Journal of Experimental Biology*, Vol. 208, No. 3, 2005, pp. 447–459. doi:10.1242/jeb.01407

[19] Dietl, J., and Garcia, E., "Stability in Ornithopter Longitudinal Flight Dynamics," *Journal of Guidance, Control, and Dynamics*, Vol. 31, No. 4, 2008, pp. 1157–1163. doi:10.2514/1.33561

[20] Doman, D., Oppenheimer, M., and Sigthorrson, D., "Dynamics and Control of a Minimally Actuated Biomimetic Vehicle: Part 1: Aerodynamic Model," *AIAA Guidance, Navigation, and Control Conference*, AIAA Paper 2009-6160, 2009.

[21] Doman, D., Oppenheimer, M., and Sigthorrson, D., "Dynamics and Control of a Minimally Actuated Biomimetic Vehicle: Part 2: Control," *AIAA Guidance, Navigation, and Control Conference*, AIAA Paper 2009-6161, 2009.

[22] Deng, X., Schenato, L., and Sastry, S., "Hovering Flight Control of a Micromechanical Flying Insect," *40th IEEE Conference on Decision and Control, Institute of Electrical and Electronics Engineers*, Orlando, FL, 2001, Paper TuA08-5.

[23] Deng, X., Schenato, L., Wu, W., and Sastry, S., "Flapping Flight for Biomimetic Robot Insects: Part 1: System Modeling," *IEEE Transactions on Robotics and Automation*, Vol. 22, No. 4, 2006, pp. 776–788. doi:10.1109/TRO.2006.875480

[24] Deng, X., Schenato, L., and Sastry, S., "Flapping Flight for Biomimetic Robot Insects: Part 2: Flight Control Design," *IEEE Transactions on Robotics and Automation*, Vol. 22, No. 4, 2006, pp. 789–803. doi:10.1109/TRO.2006.875483

[25] Schenato, L., Campolo, D., and Sastry, S., "Controllability Issues in Flapping Flight for Biomimetic Micro Air Vehicles (MAVS)," *42nd IEEE Conference on Decision and Control, Institute of Electrical and Electronics Engineers*, Mauri, HI, 2003, Paper FrE10-5.

[26] Vanella, M., Fitzgerald, T., Preidikman, S., Balaras, E., and Balachandran, B., "Influence of Flexibility on the Aerodynamic Performance of a Hovering Wing," *Journal of Experimental Biology*, Vol. 212, No. 1, 2009, pp. 95–105. doi:10.1242/jeb.016428

[27] Fitzgerald, T., Valdez, M., Vanella, M., Balaras, E., and Balachandran, B., "Flexible Flapping Systems: Computational Investigations into Fluid-Structure Interactions," *Aeronautical Journal*, Vol. 115, No. 1172, 2011,

pp. 593–604.
doi:10.1017/S000192400000628X
[28] Khan, Z., and Agrawal, S., "Modeling and Simulation of Flapping Wing Micro Air Vehicles," *ASME International Design Engineering Technical Conference*, American Soc. of Mechanical Engineers, New York, pp. 2607–2626, 2005.
[29] Gebert, G., Gallmeier, P., and Evers, J., "Equations of Motion for Flapping Flight," *AIAA Atmospheric Flight Mechanics Conference*, AIAA Paper 2002-4872, 2002.
[30] Loh, K. H., Cook, M., and Thomasson, P., "An Investigation into the Longitudinal Dynamics and Control of a Flapping Wing Micro Air Vehicle at Hovering Flight," *The Aeronautical Journal*, Vol. 107, No. 1078, 2003, pp. 743–753.
[31] Lasek, M., and Sibilski, K., "Modeling and Simulation of Flapping Wing Control for a Micromechanical Flying Insect (Entomopter)," *AIAA Modeling and Simulation Technologies Conference and Exhibit*, AIAA Paper 2002-4973, 2002.
[32] Buler, W., Loroch, L., Sibilski, K., and Zyluk, A., "Modeling and Simulation of Nonlinear Dynamic Behavior of a Flapping Wings Micro-Air-Vehicle," *42nd AIAA Aerospace Sciences Meeting and Exhibit*, AIAA Paper 2004-541, 2004.
[33] Grauer, J., and Hubbard, J., "Multibody Model of an Ornithopter," *AIAA Journal of Guidance, Control, and Dynamics*, Vol. 32, No. 5, 2009, pp. 1675–1679.
doi:10.2514/1.43177
[34] Bolender, M. A., "Rigid Multi-Body Equations-of-Motion for Flapping Wing MAVs Using Kane's Equations," *AIAA Guidance, Navigation, and Control Conference*, AIAA Paper 2009-6158, 2009.
[35] Orlowski, C. T., and Girard, A. R., "Modeling and Simulation of Nonlinear Dynamics of Flapping Wing Micro Air Vehicles," *AIAA Journal*, Vol. 49, No. 5, 2011, pp. 969–981.
doi:10.2514/1.J050649
[36] Kalmar-Nagy, T., and Stanciulescu, I., "Can Complex Systems Really be Simulated?" *Applied Mathematics and Computation*, Vol. 227, 2014, pp. 199–211.
doi:10.1016/j.amc.2013.11.037
[37] Roccia, B. A., Preidikman, S., Gebhardt, C. G., and Massa, J. C., "Dynamics of Micro-Air-Vehicles with Flapping Wings: A Multibody System Approach," *IEEE Latin America Transactions*, Vol. 11, No. 1, 2013, pp. 189–195.
doi:10.1109/TLA.2013.6502800
[38] Preidikman, S., and Mook, D. T., "Time Domain Simulations of Linear and Nonlinear Aeroelastic Behavior," *Journal of Vibrations and Control*, Vol. 6, No. 8, 2000, pp. 1135–1175.
doi:10.1177/107754630000600802
[39] Preidikman, S., "Numerical Simulations of Interactions Among Aerodynamics, Structural Dynamics, and Control Systems," Ph.D. Thesis, Virginia Polytechnic Inst. and State Univ., Blacksburg, VA, 1998.
[40] Dickinson, M. H., Lehmann, F.-O., and Sane, S. P., "Wing Rotation and the Aerodynamic Basis of Insect Flight," *Science*, Vol. 284, No. 5422, 1999, pp. 1954–1960.
doi:10.1126/science.284.5422.1954
[41] Dickinson, M. H., and Götz, K., "Unsteady Aerodynamic Performance of Model Wings at Low Reynolds Numbers," *Journal of Experimental Biology*, Vol. 174, No. 1, 1993, pp. 45–64.
[42] Konstandinopoulos, P., Mook, D. T., and Nayfeh, A. H., "A Numerical Method for General Unsteady Aerodynamics," *AIAA Atmospheric Flight Mechanics Conference*, AIAA Paper 1981-1877, 1981.
[43] Markow, T., and O'Grady, P., *Drosophila: A Guide to Species Identification and Use*, Elsevier, San Diego, CA, 2006, Chap. 2.
[44] Baruh, H., *Analytical Dynamics*, McGraw–Hill, New York, 1999, Chap. 2.
[45] Shabana, A. A., *Dynamics of Multibody Systems*, 4th ed., Cambridge Univ. Press, New York, 2013, Chap. 2, 3.
[46] Karnovsky, I. A., and Lebed, O. I., *Formulas for Structural Dynamics: Tables, Graphs and Solutions*, 1st ed., McGraw–Hill, New York, 2000.
[47] Nikravesh, P. E., *Computer-Aided Analysis of Mechanical Systems*, Prentice–Hall, New Jersey, 1988, Chap. 11.
[48] Bauchau, O. A., *Flexible Multibody Mechanics*, 1st ed., Springer, New York, 2010, Chap. 4.
[49] Heard, W. B., *Rigid Body Mechanics*, Wiley–VCH Verlag GmbH, Weinheim, Germany, 2006, Chap. 3.
[50] Baumgarte, J., "Stabilization of Constraints and Integrals of Motion in Dynamical Systems," *Computational Mathematics Applied to Mechanical Engineering*, Vol. 1, No. 1, 1972, pp. 1–16.
doi:10.1016/0045-7825(72)90018-7
[51] Ascher, U. M., and Petzold, L. R., "Stability of Computational Methods for Constrained Dynamics Systems," *SIAM Journal on Scientific Computing*, Vol. 14, No. 1, 1993, pp. 95–120.
doi:10.1137/0914007
[52] Ascher, U. M., Chin, H., and Reich, S., "Stabilization of DAEs and Invariant Manifolds," *Numerische Mathematik*, Vol. 67, No. 2, 1994, pp. 131–149.
doi:10.1007/s002110050020
[53] Ascher, U. M., Chin, H., Petzold, L. R., and Reich, S., "Stabilization of Constrained Mechanical Systems with DAEs and Invariant Manifolds," *Journal of Mechanics of Structures and Machines*, Vol. 23, No. 2, 1995, pp. 135–157.
doi:10.1080/08905459508905232
[54] Flores, P., Machado, M., and da Silva, M. T., "A Parametric Study on the Baumgarte Stabilization Method for Forward Dynamics of Constrained Multibody Systems," *Journal of Computational and Nonlinear Dynamics*, Vol. 6, No. 1, 2011, Paper 011019.
doi:10.1115/1.4002338
[55] Carnahan, B., Luther, H. A., and Wilkes, J. O., *Applied Numerical Methods*, Wiley, New York, 1969, pp. 390–392.
[56] Ascher, U. M., and Petzold, L. R., *Computer Methods for Ordinary Differential Equations and Differential-Algebraic Equations*, SIAM, Philadelphia, 1997, Chap. 10.
[57] Nikravesh, P. E., "Initial Condition Correction in Multibody Dynamics," *Multibody System Dynamics*, Vol. 18, No. 1, 2007, pp. 107–115.
doi:10.1007/s11044-007-9069-z
[58] Fry, S. N., Sayaman, R., and Dickinson, M. H., "The Aerodynamics of Hovering Flight in Drosophila," *Journal of Experimental Biology*, Vol. 208, No. 12, 2005, pp. 2303–2318.
doi:10.1242/jeb.01612
[59] Neef, M., and Hummel, D., "Euler Solution for a Finite-Span FlappingWing," *Fixed and Flapping Wing Aerodynamics for Micro Air Vehicle Applications*, edited by T. J. Muller, Vol. 195, Progress in Astronautics and Aeronautics, AIAA, Reston, VA, 2001, pp. 429–449, Chap. 19.
[60] Ansari, S. A., Żbikowski, R., and Knowles, K., "Non-Linear Unsteady Aerodynamics Model for Insect-Like Flapping Wings in the Hover. Part 1: Methodology and Analysis," *Journal of Aerospace Engineering*, Vol. 220, No. 2, 2006, pp. 61–83.
doi:10.1243/09544100JAERO49
[61] Ansari, S. A., Żbikowski, R., and Knowles, K., "Non-Linear Unsteady Aerodynamics Model for Insect-Like Flapping Wings in the Hover. Part 2: Implementation and Validation," *Journal of Aerospace Engineering*, Vol. 220, No. 3, 2006, pp. 169–186.
doi:10.1243/09544100JAERO50
[62] Birch, J. M., and Dickinson, M. H., "Spanwise Flow and the Attachment of the Leading-Edge Vortex on Insect Wings," *Nature (London)*, Vol. 412, No. 6848, Aug. 2001, pp. 729–733.
doi:10.1038/35089071
[63] Bos, F. M., Lentink, D., van Oudheusden, B. W., and Bijl, H., "Numerical Study of Kinematic Wing Models of Hovering Insect Flight," *45th AIAA Aerospace Sciences Meeting*, AIAA Paper 2007-482, 2007.
doi:10.2514/6.2007-482
[64] Ellington, C. P., "The Aerodynamics of Hovering Insects Flight. III. Kinematics," *Philosophical Transactions of the Royal Society of London. Series B, Biological Sciences*, Vol. 305, No. 1122, 1984, pp. 41–78.
doi:10.1098/rstb.1984.0051
[65] Ennos, A. R., "The Kinematics and Aerodynamics of the Free Flight of Some Diptera," *Journal of Experimental Biology*, Vol. 142, No. 1, 1989, pp. 49–85.
[66] Walker, S. M., Thomas, A. L. R., and Taylor, G. K., "Deformable Wing Kinematics in Free-Flying Hoverflies," *Journal of the Royal Society of London, Interface*, Vol. 7, No. 42, 2009, pp. 131–142.
doi:10.1098/rsif.2009.0120
[67] Roccia, B. A., Preidikman, S., Verstraete, M. L., and Mook, D. T., "Influence of Spanwise Twisting and Bending on Lift Force Generation in MAVs-Like Flapping Wings," *Journal of Aerospace Engineering (ASCE)*, Vol. 30, No. 1, 2017, pp. 1–15.
doi:10.1061/(ASCE)AS.1943-5525.0000677
[68] Lighthill, M. J., "A New Approach to Thin Airfoil Theory," *The Aeronautical Quarterly*, Vol. 3, No. 3, 1951, pp. 193–210.
doi:10.1017/S0001925900000639
[69] Katz, J., and Plotkin, A., *Low-Speed Aerodynamics*, 2nd ed., Cambridge Univ. Press, New York, 2001, pp. 421–495.
[70] Sane, S. P., "The Aerodynamics of Insect Flight," *Journal of Experimental Biology*, Vol. 206, No. 23, 2003, pp. 4191–4208.
doi:10.1242/jeb.00663

Downloaded by UNIVERSITY OF MARYLAND on June 12, 2017 | http://arc.aiaa.org | DOI: 10.2514/1.J055137

[71] Ehlers, F. E., and Manro, M. E., "A Method for Computing the Leading-Edge Suction in a Higher-Order Panel Method," NASA Contractor Rept. 3730, 1984.
[72] Sun, M., and Xiong, Y., "Dynamic Flight Stability of a Hovering Bumblebee," *Journal of Experimental Biology*, Vol. 208, No. 3, 2005, pp. 447–459. doi:10.1242/jeb.01407
[73] Taylor, G. K., and Thomas, A. L. R., "Dynamic Flight Stability in the Desert Locust Schistocerca Gregaria," *Journal of Experimental Biology*, Vol. 206, No. 16, 2003, pp. 2803–2829. doi:10.1242/jeb.00501
[74] Koumoutsakos, P., "Multiscale Flow Simulations Using Particles," *Annual Review of Fluid Mechanics*, Vol. 37, No. 1, 2005, pp. 457–487. doi:10.1146/annurev.fluid.37.061903.175753
[75] Winckelmans, G. S., and Leonard, A., "Contributions to Vortex Particle Methods for the Computation of Three-Dimensional Incompressible Unsteady Flows," *Journal of Computational Physics*, Vol. 109, No. 2, 1993, pp. 247–273. doi:10.1006/jcph.1993.1216
[76] Greengard, L., and Rohklin, V., "A Fast Algorithm for Particle Simulations," *Journal of Computational Physics*, Vol. 135, No. 2, 1997, pp. 280–292. doi:10.1006/jcph.1997.5706
[77] Géradin, M., and Cardona, A., *Flexible Multibody Dynamics — A Finite Elements Approach*, Wiley, New York, 2001, pp. 105–136.

H. Blackburn
Associate Editor

Downloaded by UNIVERSITY OF MARYLAND on June 12, 2017 | http://arc.aiaa.org | DOI: 10.2514/1.J055137